A&A 545, A35 (2012)
DOI: 10.1051/0004-6361/201219544

Astronomy & Astrophysics

The X-ray lightcurve of Sagittarius A* over the past 150 years inferred from Fe-Kα line reverberation in Galactic centre molecular clouds

R. Capelli[1], R. S. Warwick[2], D. Porquet[3], S. Gillessen[1], and P. Predehl[1]

[1] Max-Planck-Institut für extraterrestrische Physik, Postfach 1312, Giessenbachstr., 85741 Garching, Germany
e-mail: `capelli@mpe.mpg.de`
[2] Department of Physics and Astronomy, University of Leicester, Leicester LE1 7RH, UK
[3] Observatoire Astronomique de Strasbourg, Université de Strasbourg, CNRS, UMR 7550, 11 rue de l'Université, 67000 Strasbourg, France

Received 4 May 2012 / Accepted 26 June 2012

ABSTRACT

Context. The spatial distribution and variability of Fe-Kα emission from molecular clouds in the Galactic centre region may provide an important key to the understanding of the recent history of Sgr A*. A very plausible interpretation is that this variability represents an echo in the reflected radiation from the clouds of a past episode of high activity in Sgr A*.

Aims. We examine the temporal and spectral properties of nine Fe-Kα bright molecular clouds (three of which newly studied) within about 30 pc of Sgr A*, in order to understand and constrain the primary energising source of the Fe fluorescence.

Methods. We collected all the archival *XMM-Newton* observations targeted at Sgr A*. The variability of the Fe-Kα line at 6.4-keV in specific cloud regions was investigated by spectrally fitting the data derived from the EPIC MOS cameras, after subtracting a modelled background. We have also studied the reflection imprints in time-averaged pn-spectra of each cloud. This involved measuring the equivalent width (EW) of the 6.4 keV line with respect to the underlying scattered continuum and the optical depth of the Fe-K absorption edge at 7.1 keV, superimposed on this same continuum. Finally we stacked the MOS spectra from two extended regions in order to quantify the east-west asymmetry apparent in the low-surface brightness diffuse Fe-Kα line emission.

Results. Significant Fe-Kα variability was detected, with a spatial and temporal pattern consistent with that reported in previous studies. The main breakthrough that sets our paper apart from earlier contributions on this topic is the direct measurement of the column density and the Fe abundance of the MCs in our sample. All the spectra were characterised by a high EW of the Fe-Kα line and the presence of absorption at the Fe-K edge, both of which serve as tracers of X-ray illumination. We used the EW measurements to infer the average Fe abundance within the clouds to be 1.6 ± 0.1 times solar. The cloud column densities derived from the spectral analysis were typically of the order of 10^{23} cm^{-2}, which is significantly higher than previous estimates. This in turn has a significant impact on the inferred geometry and time delays within the cloud system. The measured cloud parameters were used to set constraints on the past activity of Sgr A* and to investigate whether a contribution to the Fe fluorescence by cosmic-ray bombardment is plausible.

Conclusions. Past X-ray activity of Sgr A* is the most likely source of ionisation within the molecular clouds in the innermost 30 pc of the Galaxy. In this scenario, the X-ray luminosity required to excite these reflection nebulae is of the order of 10^{37}–10^{38} erg s^{-1}, significantly lower than that estimated for the Sgr B2 molecular cloud. Moreover, the inferred Sgr A* lightcurve over the past 150 years shows a long-term downwards trend punctuated by occasional counter-trend brightening episodes of at least 5 years duration. Finally, we found that a contribution to the Fe fluorescence by X-ray transient binaries and cosmic-ray bombardment are very likely, and suggest possible ways to study this latter phenomenon in the near future.

Key words. ISM: clouds – cosmic rays – Galaxy: center – X-rays: ISM

1. Introduction

The Galactic centre (GC) region is a unique environment within the local Universe, which provides many tests of our understanding of fundamental issues in astrophysics. The region hosts the nearest super massive black hole (SMBH), Sgr A*, with a mass of 4×10^6 $M_\odot$ (Schödel et al. 2002; Ghez et al. 2008). It is also a region in which high energy phenomena abound. For example, in X-rays the Sgr B2 and Sgr C molecular complexes, located at projected distances of 90 pc and 70 pc from Sgr A*, shine brightly through 6.4-keV Fe-Kα line emission (Koyama et al. 1996; Murakami et al. 2000; Nakajima et al. 2009), consistent with the prediction of Sunyaev et al. (1993).

The physical mechanism responsible for the Fe-Kα emission from these molecular clouds near the GC is the fluorescence of cold, neutral or near-neutral matter irradiated by high energy particles or X-ray photons. So far several hypotheses have been proposed as to the nature and origin of the primary source of this irradiation. The possibilities include: the X-ray reflection nebulae model (XRN, Sunyaev & Churazov 1998), heating by low-energy cosmic-rays (CR; Yusef-Zadeh et al. 2002), shock mechanisms (Yusef-Zadeh et al. 1997), and electron bombardments (Predehl et al. 2003). A recent suggestion is that subrelativistic protons can be created via accretion of stellar debris onto the central black hole, thus explaining both the observed X-ray continuum and the 6.4 keV line emission from the GC

(Dogiel et al. 2009). Other particle-like candidates can be CR electrons originating in supernova events (Valinia et al. 2000).

If the fluorescence observed in molecular complexes is the result of irradiation by X-ray photons, a luminous localised source of X-rays must be invoked to power the observed emission, since the diffuse hot plasma which permeates the central regions of the Galactic plane produces a factor ten less photons than is required to account for the observed Fe-Kα flux. It has been estimated that, depending on its position relatively to the Sgr B2 and Sgr C molecular clouds, this source should have a 2–10 keV luminosity of the order of 10^{39} erg s^{-1}. Presently no persistent sources in the GC region have such a high luminosity; however a past transient outburst in a source, which has now returned to a relatively quiescent state, might well match the requirement. Sgr A* itself is arguably the best candidate, since although its activity is currently rather weak (the brightest flare measured with *XMM-Newton* has a luminosity of the order of a few 10^{35} erg s^{-1}, Porquet et al. 2003), the SMBH could have undergone a period of high-state activity in the past (Koyama et al. 1996). In fact, the projected light travel time to Sgr B2 implies an outburst roughly 75–150 years ago, according to a recent estimate (Terrier et al. 2010). Since there are a number of filaments nearer to Sgr A* which emit at 6.4-keV, the same argument would require Sgr A* to also have flared more recently, say within the last 100 years, depending on the relative position of the clouds along the line of sight.

One method of distinguishing between the point source and the particle hypothesis is to investigate the lightcurve of the filaments which emit the 6.4-keV line. If we are dealing with a transient source as an engine of the fluorescent emission, one might expect the temporal evolution of the observed line flux to follow the light curve of the outburst, subject to blurring arising from the spread in light-travel delays inherent in the source to cloud geometry. Such effects have been found in the Sgr B2 molecular cloud where the brightest peak of the Fe-Kα emission observed in 1995 by ASCA (Koyama et al. 1996; Murakami et al. 2000) maintained the same brightness level when remeasured in 2000 with *Chandra* (Murakami et al. 2001) but then, some five years later when observed by *Suzaku*, showed a marked decline to approximately half the peak value (Koyama et al. 2008; Inui et al. 2009). Similarly, Nakajima et al. (2009) discovered variability of the Fe-Kα flux from Sgr C on the basis of recent Sukaku observations. Moreover, Muno et al. (2007) have reported the evolution in intensity and morphology of the 4–8 keV continuum emission in two filamentary regions located close to Sgr A*. The latter changes occurred on parsec scales (in projection), which requires a brightening/fading of the illuminating source over a 2–3 year period, with an inferred 2–8 keV luminosity of at least 10^{37} erg s^{-1}. Recently, Ponti et al. (2010) showed that the 6.4 keV line flux from the molecular filaments with 15 arcmin of Sgr A* exhibit a complex pattern of variability. If these molecular clouds/knots have a particular distribution along the line of sight, then it is possible to argue that they were all energised by the same outburst on Sgr A*, consistent with the XRN scenario (Ponti et al. 2010). However, given the observational complexities, it is very possible that this is not the complete story; indeed, very recently Capelli et al. (2011b) studied the Fe-Kα line emission from the MCs in the Arches cluster region (about 20 pc in projection from Sgr A*), showing that the XRN/Sgr A* scenario can hardly describe the spectral and temporal properties of those clouds.

The above results open once more the question whether Sgr A* has exhibited AGN activity in the past and, if so, what is the exact nature of that activity. It is in this context that we reassess in this paper, the morphology, variability and spectral properties of the 6.4-keV emitting clouds within 15′ of Sgr A*, using the extensive set of *XMM-Newton* observations targeted at this region. Our goal is to investigate both the past role of Sgr A* (or other transient sources) in illuminating the GC molecular clouds and also to seek evidence for a contribution from alternative mechanisms, such as CR bombardment, in the excitation of the Fe fluorescence which characterises the GC environment. Throughout this work, the distance to the GC has been taken to be 8 kpc (Gillessen et al. 2009).

2. Observations and data reduction

We checked in the HEASARC archive for *XMM-Newton* observations of the GC region and selected observations with a nominal pointing position within 15′ from Sgr A* (RA = $17^h45^m40.045^s$, Dec = –29°0′27.9″). Data from the EPIC cameras, consisting of one PN back illuminated CCD detector (Strüder et al. 2001) and two MOS front illuminated CCD detectors (Turner et al. 2001), have been reprocessed using the tasks EMPROC and EPPROC in the Science Analysis Software SAS version 9.0. For our purposes it is necessary to rigorously select the good time intervals (GTI), representing the periods in which the internal background of the cameras was relatively quiescent. For this reason we used the SAS task ESPFILT to screen data with a high particle-induced background. This task was originally developed inside the Extended Sources Analysis Software (ESAS, Snowden et al. 2004) and then converted into a specific procedure in the SAS. This task fits a Gaussian peak to the distribution of count rates, and creates a GTI for those time intervals with count rates within the thresholds, defined to be $\pm1.5\sigma$ from the mean count rate. The GTI filtering has been done separately for all the three EPIC cameras. Figure 1 shows the results for the screening done on the MOS1 data of OBSID 0202670701, and how the task operates. The upper panel shows the histogram for the full field of view (FOV) lightcurve in the 2.5–12 keV band, while in the middle and the lower panels are, respectively, the 2.5–8.5 keV lightcurve of the IN FOV region and the corner data. The green time intervals are those selected by the filtering process and used for the further analysis. The results of the screening done on all the selected data sets together with the specifics of each observation are reported in Table 1.

We performed a different GTI selection for OBSIDs 0402430301, 0402430401 and 0505670101, which were contaminated by very high radiation levels towards the end of the respective observations. Indeed, the filtering approach of selecting the count rate inside $\pm1.5\sigma$ from the mean count rate can lead to a bias in the case of a very strong flare during an observation (especially for the PN camera; this does not influence the MOS cameras). Moreover when removing the count rates below the mean count rate-1.5σ (see Fig. 1) all the genuine low background exposure times in the observation are removed. The ESPFILT filtered PN event files for OBSIDs 0402430301, 0402430401 and 0505670101 have a GTI exposure of 0.3, 4.3 and 9.2 ks, respectively. We built the 10–12 keV lightcurve of the full FOV for these OBSIDs, and selected those intervals with a count rate lower than 1.5 counts s^{-1} (for OBSIDs 0402430301 and 0402430401) and 1.25 counts s^{-1} (OBSID 0505670101). The total exposures in the PN cameras of these OBSIDs with the new filtering process are 61.5, 48.9 and 74.2 ks, respectively.

Throughout our analysis we have only selected single and double events (PATTERN $\leq$ 4) for PN and up to quadruple events (PATTERN $\leq$ 12) for MOS1 and MOS2 cameras. For all the

Table 1. Specifications for the selected OBSIDs: MODE/FILTER combination used for each of the pointings, and GTI compared to the total exposure for each instrument.

		Instrument specifics			GTI & Exposure (ks)		
OBSID	Obs Date yyyy-mm-dd	PN mode/filter	MOS1 mode/filter	MOS2 mode/filter	PN GTI/exp	MOS1 GTI/exp	MOS2 GTI/exp
0111350101	2002-02-26	F/T	F/M	F/M	38.590/40.030	42.262/52.105	41.700/52.120
0202670501	2004-03-28	E/M	F/M	F/M	13.320/101.170	33.070/107.784	30.049/108.572
0202670601	2004-03-30	E/M	F/M	F/M	25.680/112.204	32.841/120.863	35.390/122.521
0202670701	2004-08-31	F/M	F/M	F/M	59.400/127.470	80.640/132.469	84.180/132.502
0202670801	2004-09-02	F/M	F/M	F/M	69.360/130.951	94.774/132.997	98.757/133.036
0402430301	2007-04-01	F/M	F/M	F/M	61.465/101.319	61.002/93.947	62.987/94.022
0402430401	2007-04-03	F/M	F/M	F/M	48.862/93.594	40.372/97.566	41.317/96.461
0402430701	2007-03-30	F/M	F/M	F/M	32.337/32.338	26.720/33.912	27.685/33.917
0505670101	2008-03-23	F/M	F/M	F/M	74.216/96.601	73.662/97.787	74.027/97.787
0554750401	2009-04-01	F/M	F/M	F/M	30.114/38.034	32.567/39.614	33.802/39.619
0554750501	2009-04-03	F/M	F/M	F/M	36.374/42.434	41.376/44.016	41.318/44.018
0554750601	2009-04-05	F/M	F/M	F/M	28.697/32.837	37.076/38.816	36.840/38.818

Notes. F = full frame MODE; E = extended full frame MODE; T = thick filter; M = medium filter. OBSID 0506291201 has PN in timing MODE.

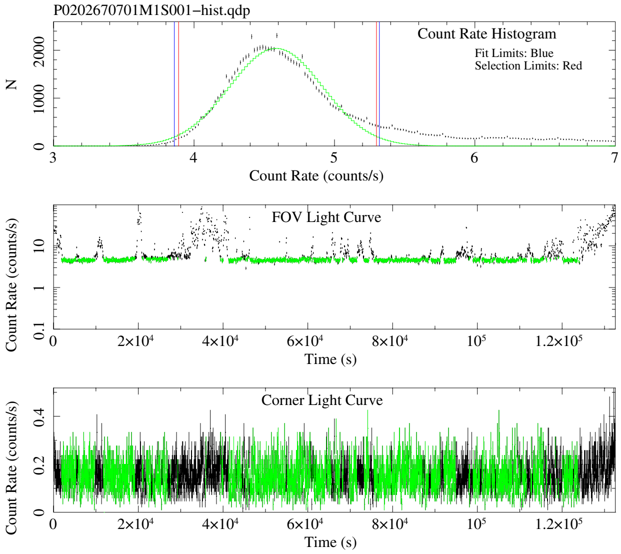

Fig. 1. Soft proton flare filtering of the MOS1 dataset from OBSID 0202670701. *Upper panel*: 2.5–12 keV count rate histogram. The blue lines mark the region used in the Gaussian fit, the green line represents the best fit Gaussian and the red lines show the bounds used to filter the data. *Mid panel*: 2.5–8.5 keV lightcurve of the IN FOV region. *Lower panel*: 2.5–8.5 keV lightcurve of the corner data. In both the Mid and the Lower panels, the points coloured green in the lightcurves correspond to the selected GTI intervals (see text).

instruments a further screening for good events was done selecting only events marked as real X-rays (FLAG==0).

3. Spatial and spectral characterisation of the Fe-Kα emission

3.1. Imaging

3.1.1. Method

First we built a fluence (integrated flux over time) map for the Fe-Kα line in a very narrow energy window in order to identify and locate the brightest Fe fluorescence regions. We proceeded by merging all the GTI filtered event files for the three EPIC cameras (where available) for every OBSID selected (see Table 1), using the SAS task EMOSAIC. In building the image of the Fe-Kα emission, we assumed a value of $E/\Delta E = 50$ for the spectral resolution (FWHM) of both PN and MOS1&2 at 6.4 keV, corresponding to a bandpass for the Fe fluorescence signal of 6336–6464 eV.

An important issue for our analysis is the subtraction of instrument background and, where appropriate, the continuum underlying the line emission. To quantify the percentage of counts in the narrow band 6336–6464 eV due to both components, we selected the energy range 3904–6208 eV in the total event file and produced 18 adjacent images of the whole FOV, each 128 eV broad. The spectral window thereby encompassed is free of contamination by strong emissions lines, including both the Fe-Kα emission from neutral or near-neutral ions and the Fe-K emission from high ionisation lines which characterise the GC high-energy thermal components. We then fit the distribution of counts as a function of the energy with a powerlaw of the form $E^{-\Gamma}$, and further used this best fit to infer the number of counts in the continuum for the images in the ranges 6208−6336 eV and 6336−6464 eV. Finally, we used the 6272 eV centered image properly scaled as background for the Fe-Kα map.

3.1.2. Results

The background- and continuum-subtracted narrow-band (6336–6464 eV) image produced by the method outlined in the previous section, in effect, represents a Fe-Kα line fluence map (with the provision that the effective exposure varies somewhat over the field). This image is shown in Fig. 2. The morphology of the Fe Kα emission evident in this image is consistent with that reported earlier by other X-ray satellites including ASCA (Koyama et al. 1996), *Chandra* (Yusef-Zadeh et al. 2007a), and *Suzaku* (Koyama et al. 2006). The main differences arise because of instrumental effects (different angular resolution and sensitivity in the hard X-ray domain) or different exposure times. Our results are also in good agreement with those reported recently by Ponti et al. (2010), based on an independent analysis of a broadly similar set of *XMM-Newton* observations.

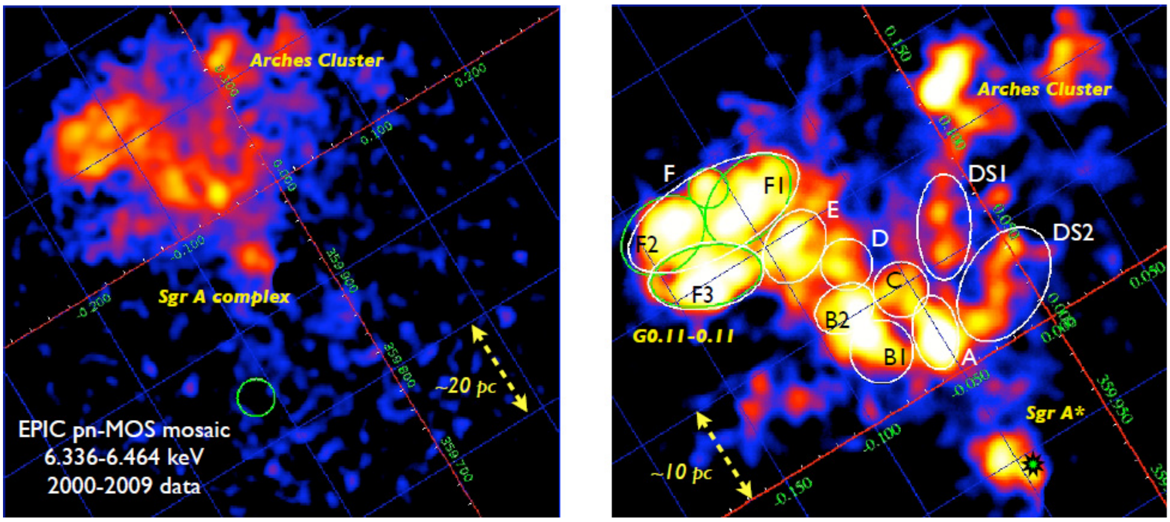

Fig. 2. *Left panel*: fluence map (6.336–6.464 keV) of the Fe-Kα emission from the filaments in the GC. The image has been smoothed with a 8-pixel diameter top-hat filter. The grid lines define the Galactic coordinate frame, where the green circle shows the background region selected for the spectral analysis of the clouds marked in the *right panel* (Sect. 3.3). *Right panel*: a zoom-in on the region of the bright filaments. The white (green) ellipses show the regions (sub-regions) selected for the spectral analysis (see Table 2); region B has been divided into two subregions B1 and B2; region F (G0.11-0.11) into three subregions, F1 (ellipse plus small circle), F2 and F3. The position of Sgr A* is marked by a green star at $l = -0.056$ deg and $b = -0.046$ deg.

The maps clearly show an asymmetry in the distribution of the Fe-Kα emission with respect to the position of Sgr A*, with all the bright filaments located to the east of Sgr A*, at negative Galactic latitudes. On the western side of the GC region, the closest molecular complex bright in Fe fluorescent lines is Sgr C, located at a projected distance from Sgr A* of approximately 70 pc. Looking at the radio maps of the GC region in CO (Oka et al. 1998) and CS (Tsuboi et al. 1999) rotational lines, an asymmetry in the distribution of molecular matter is very noticeable, with more concentrated to the east of Sgr A*. Nevertheless, a certain amount of cold matter not shining in the 6.4-keV line is present along the whole plane of the Galaxy, and this should be taken into account in explaining the origin of the Fe-Kα emission in the filaments between Sgr A* and the GC feature known as the Radio Arc. Looking at the left panel in Fig. 2, the presence of low surface brightness 6.4-keV line emission is evident across the whole region between the Radio Arc ($l \approx 0.2°$) and Sgr A* (coded as diffuse blue in Fig. 2). In contrast, this low-level emission is largely absent at negative longitudes. We emphasise that this is not an image artifact. In fact, the 6.4-keV spatial distribution at faint levels coincides remarkably well with the contours of TeV γ-ray emission measured by HESS (Aharonian et al. 2006), a connection first noted by Yusef-Zadeh et al. (2007a) using the 6.4-keV line equivalent-width image measured by *Chandra*. Thanks to the much higher effective area of *XMM-Newton*, we are now able to establish that this strong correlation apparently extends to regions outside of those occupied by very dense molecular clouds (see Sect. 6).

The bright region in Fig. 2 located at $l \sim 0.12°$, $b \sim 0.05°$ is the Arches Cluster; for the study of the 6.4-keV line emission from the MCs in this region we cross refer to the recent work by Capelli et al. (2011b). We have excluded from our study the bright feature at $l \sim -0.05°$. This is the Sgr A complex, containing both Sgr A* itself and the Sgr A east supernova remnant (SNR). In Table 2 we report the coordinates and the sizes of the selected regions of elliptical shape upon which our spectral analysis is based. We selected these sky regions solely on the basis of Fe-Kα morphology without reference to potential radio molecular counterparts (that could help to identify spatially and physically connected regions). In doing so, we neglected the possibility that some of the filaments which are bright in the Fe-Kα line could be part of a single, more extended, molecular complex.

3.2. Spectroscopy: studying the Fe-Kα variability

3.2.1. Method

We carried out a spectroscopic analysis of the Fe-Kα bright filaments shown in Fig. 2, with the objective of measuring the photon flux in the 6.4 keV line and searching for any variations in this quantity over an eight-year timeframe. The molecular complexes bright in the Fe fluorescent line are embedded in strong X-ray emission due to the presence along the line of sight of unresolved thermal X-ray emission. This thermal emission, which permeates the whole GC region can be characterised as a two-temperature plasma with typically $kT_1 \approx 1$ keV and $kT_2 \approx 6.5$ keV (Koyama et al. 2007). For our purposes, everything but the 6.4-keV line emission is considered as background radiation. Unfortunately due to the relatively low surface brightness of the fluorescent emission and the spatial variations inherent in the foreground emission, the subtraction of a "local background" introduces many systematics in the resultant spectrum. Therefore, we adopted the approach of modelling the Non X-ray Background (NXB) rather than subtracting it. In Appendix A we describe the different ways of dealing with NXB in an *XMM-Newton* dataset, and specify the methodology we actually employed. One consequence of the use of the background modelling technique was that for this part of analysis we were restricted to the use of the MOS data only.

We built response and ancillary files with the SAS tasks RMFGEN v1.55.1 and ARFGEN v1.76.4. No point source excision has been applied. The need for a systematic analysis with spectra encompassing very different exposure times and net counts, led us to use the Cash statistic (Cash 1979) rather than χ^2.

Table 2. Central position, sizes (radius or semi-axis) and projected distance from Sgr A* of the regions and sub-regions selected for the spectral analysis (see Fig. 2).

Region	Ponti	RA (J2000)	Dec (J2000)	Size (arcmin)	d_{proj} (pc)
The 9 clouds					
A	MC1	17:45:52.398	–28:56:38.15	0.65×1.08	10.9
B1	MC2	17:45:59.592	–28:57:10.09	0.91×0.91	12.6
B2	1&2*	17:46:04.394	–28:55:56.74	0.90×0.68	16.3
C	new	17:45:57.026	–28:55:22.91	0.8×0.8	14.7
D	3&4*	17:46:04.252	–28:54:39.64	0.75×0.75	18.3
E	5*	17:46:10.997	–28:54:09.50	1.12×0.83	21.6
F	G0.11-0.11	17:46:21.627	–28:53:11.36	2.75×1.22	27.2
		17:46:22.615	–28:55:00.14	1.68×0.95	
DS1	new	17:45:51.294	–28:53:35.76	0.77×1.52	17.0
DS2	new	17:45:43.377	–28:55:14.99	1.78×1.16	12.3
The 3 F subregions					
F1		17:46:17.084	–28:52:49.45	1.49×1.01	–
		17:46:22.443	–28:52:26.99	0.59×0.59	–
F2		17:46:28.297	–28:53:50.10	1.32×1.01	–
F3		17:46:22.615	–28:55:00.14	1.68×0.95	–
Large regions					
EDE		17:45:53.128	–28:52:26.19	10.95×7.09	–
EDW		17:45:13.233	–29:06:46.85	10.95×7.09	–

Notes. Note that region F (G0.11-0.11) and also sub-region F1 are comprised of two separate components. A cross-reference to the cloud designation employed by Ponti et al. (2010) is also provided. The clouds marked with a star are subregions of the *Bridge* feature identified by Ponti et al. (2010).

We grouped the channels in each spectrum with the GRPPHA tool to ensure at least 1 count/bin.

We fitted all the spectra with a model which accounts for all of the source and instrumental components. The former includes the two thermal components noted above, a power-law continuum plus an associated 6.4-keV Fe line (representing reflection and fluorescence in the clouds). We use a second power-law component to model a defined contribution from the instrument background, which is not subject to the instrument response (see Appendix A). For a more detailed description of these spectral components see Capelli et al. (2011b). Note that in this analysis we fixed the temperature of the hot plasma in every spectrum to 6.5 keV (Koyama et al. 2007) since this is critical in obtaining a consistent measurement of the Fe-Kα line flux across all the spectra (different instruments/epochs).

Throughout our spectral analysis we have considered only observations with an exposure longer than 30 ks. If different datasets were part of a set of observations carried out over a couple of days, the associated spectra were added together with the ftool MATHPHA, with the same done for the response files using the ftools ADDARF and ADDRMF. Errors have been considered at the 90% confidence level. The resulting temporal sampling was as follows: the OBSIDs 0111350101 (Feb02), 0202670501 + 0202670601 (Mar04), 0202670701 + 0202670801 (Sep04), 0402430301 + 402430401 + 402430701 (Apr07), 0505670101 (Mar08), 054750401 + 0554750501 + 0554750601 (Apr09). A typical result from this spectral modelling process is illustrated in Fig. 3.

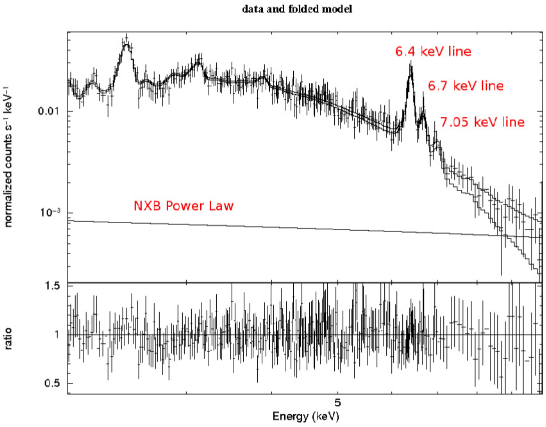

Fig. 3. *Upper panel*: the spectrum derived for Region B1 from the September 2004 MOS1 dataset together with the best-fitting spectral model. The lower solid line shows the NXB power-law component. The two curves show the net X-ray source spectrum and the source plus NXB best fit model (top curve). Three Fe lines are labelled; neutral Fe-Kα and Kβ lines at 6.4 and 7.05 keV, and the Fe XXV Kα line at 6.7 keV. *Lower panel*: ratio between the spectral points and the best fit model.

3.2.2. Results

Our goal is to study the temporal behaviour of the Fe fluorescence in the filaments with a view to constraining the nature and location of the energising source. For example, a clear spatial pattern to the variations might, in principle, help us identify a preferred direction for the incoming photons/particles. The 6.4-keV line fluxes derived from our spectral analysis for the selected regions in the different observing periods are presented in Table 3. Here the measurements are calculated as the weighted mean of the MOS1&2 values with the errors representing the 90% confidence range. Figure 4 shows the resulting Fe-Kα flux lightcurves for the different regions covering the period 2002–2009. In each of the selected regions the surface brightness of the 6.4-keV line lies in the range 5–10×10^{-6} photons cm^{-2} s^{-1} arcmin^{-2}; from the lightcurves it is clear that some regions show evidence of substantial variability, while some others appear to remain roughly constant. To quantify this, we fitted the 6.4-keV line fluxes as a linear function of time t:

$$F_{64} = A + B\,t,$$

Table 3. Fluxes of the Fe-Kα line in units of 10^{-5} photons cm^{-2} s^{-1}.

Region	Feb. 02	Mar. 04	Sep. 04	Apr. 07	Mar. 08	Apr. 09
A	2.5 ± 0.3	2.2 ± 0.2	2.1 ± 0.1	2.2 ± 0.2	2.2 ± 0.2	2.2 ± 0.2
B1	2.3 ± 0.3	1.7 ± 0.2	1.5 ± 0.1	1.6 ± 0.1	1.3 ± 0.2	1.2 ± 0.1
B2	0.9 ± 0.2	0.7 ± 0.2	1.1 ± 0.1	2.1 ± 0.2	2.1 ± 0.2	2.1 ± 0.2
C	0.8 ± 0.3	0.7 ± 0.2	0.9 ± 0.2	1.2 ± 0.2	1.1 ± 0.3	1.2 ± 0.2
D	0.5 ± 0.2	0.7 ± 0.2	0.8 ± 0.1	1.0 ± 0.1	1.1 ± 0.2	2.1 ± 0.2
E	2.4 ± 0.4	2.2 ± 0.3	1.8 ± 0.2	2.1 ± 0.2	2.2 ± 0.3	2.1 ± 0.2
F	13.1 ± 1.0	11.2 ± 0.8	11.4 ± 0.5	10.0 ± 0.5	9.4 ± 0.7	9.1 ± 0.5
F1	4.4 ± 0.6	4.0 ± 0.5	4.4 ± 0.3	3.4 ± 0.3	3.0 ± 0.4	3.4 ± 0.3
F2	4.1 ± 0.6	3.1 ± 0.4	3.6 ± 0.3	3.7 ± 0.3	3.3 ± 0.4	2.6 ± 0.3
F3	5.2 ± 0.6	4.2 ± 0.5	3.8 ± 0.3	3.5 ± 0.3	3.4 ± 0.4	3.4 ± 0.3
DS1	1.5 ± 0.3	1.5 ± 0.3	1.4 ± 0.1	1.4 ± 0.1	1.4 ± 0.2	1.4 ± 0.2
DS2	2.8 ± 0.4	2.3 ± 0.3	2.4 ± 0.2	2.1 ± 0.2	2.4 ± 0.2	2.5 ± 0.2

Notes. The values are the weighted mean of the MOS1&2 measured fluxes. The different columns refer to different datasets (see text). The Apr07, Mar08 and Apr 09 fluxes for the regions D, DS1 and DS2 are based on MOS 2 data only, as a consequence of the damaged sustained by CCD6 in MOS 1 on 9 March 2005 (Abbey et al. 2006).

where $B > 0$ indicates an increasing Fe-Kα flux (F_{64}). Table 4 reports the results for the selected regions and in Fig. 4 we show the best fit linear functions overplotted on the lightcurves, where the error bars represent (for this case only) the 1σ uncertainty as used for the calculation of the $\chi^2_{\rm red}$. From this it is clear that the temporal behaviour of the Fe-Kα flux differs markedly from filament to filament. In brief, the different regions exhibit the following behaviour:

*R*egion A: the Fe-Kα flux measured in this molecular complex does not show any significant variability on a timescale of 8 years. The weighted mean flux across the full set of observations is $2.16 \pm 0.07 \times 10^{-5}$ photons cm^{-2} s^{-1}, which translates to a surface brightness of $9.9 \pm 0.03 \times 10^{-6}$ photons cm^{-2} s^{-1} arcmin^{-2}.

Region B1: we have measured a decrease of the 6.4-keV flux from the sub-region B1 at a confidence of 4.3σ, although a linear decrease does not provide a satisfactorily description of the light curve ($\chi^2_{\rm red} = 1.46$, see Table 4). The rate of decrease of the Fe-Kα line flux in this cloud is $8.1 \pm 3.1 \times 10^{-7}$ photons cm^{-2} s^{-1} year^{-1}.

Region B2: we have measured a strong increase of the Fe Kα flux from the region B2 with a 11.9σ confidence, although the high value of the $\chi^2_{\rm red}$ (8.1) for the fit suggests that this rise may not be truly linear. The measured rate of increase of the Fe-Kα line flux is $2.4 \pm 0.3 \times 10^{-6}$ photons cm^{-2} s^{-1} year^{-1}.

Region C: the Fe-Kα flux from region C has been measured to have an increase at 4.3σ confidence with the overall $\chi^2_{\rm red}$ for the best fit linear function being 1.2. The rate of increase of the Fe-Kα line flux is $7 \pm 4 \times 10^{-7}$ photons cm^{-2} s^{-1} year^{-1}. Looking at the lightcurve in greater detail, we notice that there is a step-wise change at roughly the mid-way point, with the weighted means for two segments being, respectively, 0.8 ± 0.1 and $1.2 \pm 0.1 \times 10^{-5}$ photons cm^{-2} s^{-1}. Region C encompasses the position of a known X-ray transient, XMMU J174554.4-285456 (Porquet et al. 2005), located at the north-west edge of the circle region. This spatial coincidence and the possibility that the transient is the illumination source for the Region C cloud will be discussed later (Sect. 7.1.1).

Region D: we have measured a rapid increase of the 6.4-keV flux from region D with a confidence of 9.5σ. The rate of growth of the Fe-Kα line flux in this region is $1.6 \pm 0.3 \times 10^{-6}$ photons cm^{-2} s^{-1} year^{-1}. In the lightcurve of region D three of the six points are not fitted by the best fit function (see Fig. 4, fourth panel); this translates into a high $\chi^2_{\rm red}$ value (9.3, Table 4) suggesting the behaviour is not well represented by a simple linear increase.

Region E: the Fe-Kα flux measured in this molecular complex is rather constant over a period of 8 years; given the high $\chi^2_{\rm red}$ of the best fit for the lightcurve of this region ($\chi^2_{\rm red} = 2.9$), we cannot exclude minor excursions of the flux. The weighted mean flux over the set of observations is $2.1 \pm 0.1 \times 10^{-5}$ photons cm^{-2} s^{-1}, which translates to a surface brightness of $7.24 \pm 0.03 \times 10^{-6}$ photons cm^{-2} s^{-1} arcmin^{-2}.

Region F: this is the region for which the measurements are most precise. The Fe-Kα flux shows a clear decrease with a 7.3σ confidence; the $\chi^2_{\rm red}$ value of the best fit function is 0.3, strongly confirming the measured decrease and constraining the functional shape of this decrease to be linear. The rate of decrease of the Fe-Kα line flux is $5.1 \pm 1.2 \times 10^{-6}$ photons cm^{-2} s^{-1} year^{-1}. To improve the spatial resolution, we have divided this region into three sub-regions and studied these separately.

Sub-regions F1-F2-F3: we have measured a decrease of the 6.4-keV line flux from all three sub-regions with a confidence of 4.8, 3.4 and 4.2σ respectively. The corresponding rates of decrease are 2.1 ± 0.7, 1.5 ± 0.7 and $1.7 \pm 0.7 \times 10^{-6}$ photons cm^{-2} s^{-1} year^{-1}. The $\chi^2_{\rm red}$ values of the best fit linear functions are, respectively, 1.3, 3.6 and 1.6; confirming the decrease is a linear function of time. Moreover we point out that the rates of decrease from the three sub-regions are compatible with each other. The agreement between the temporal behaviour of both the whole complex and the individual subregions suggests a common origin for the Fe-Kα emission within a single large molecular structure, i.e. the G0.11$-$0.11 molecular cloud (Yusef-Zadeh et al. 2002). Tsuboi et al. (1997) have show that this molecular complex has a shell-like structure that may be interacting with the western vertical filaments of the Radio Arc. Thus, G0.11$-$0.11 could host an extended high energy particle accelerator/decelerator.

Regions DS1 and DS2: both the low surface brightness regions DS1 and DS2 show a constant 6.4-keV line signal over a period of 8 years. The weighted mean flux within this set of observations is 1.42 ± 0.07 and $2.33 \pm 0.09 \times 10^{-5}$ photons cm^{-2} s^{-1} respectively, which translates into a surface brightness of 3.8 ± 0.2 and $3.6 \pm 0.1 \times 10^{-6}$ photons cm^{-2} s^{-1} arcmin^{-2}. The $\chi^2_{\rm red}$ values make us confident of the constant nature of the light

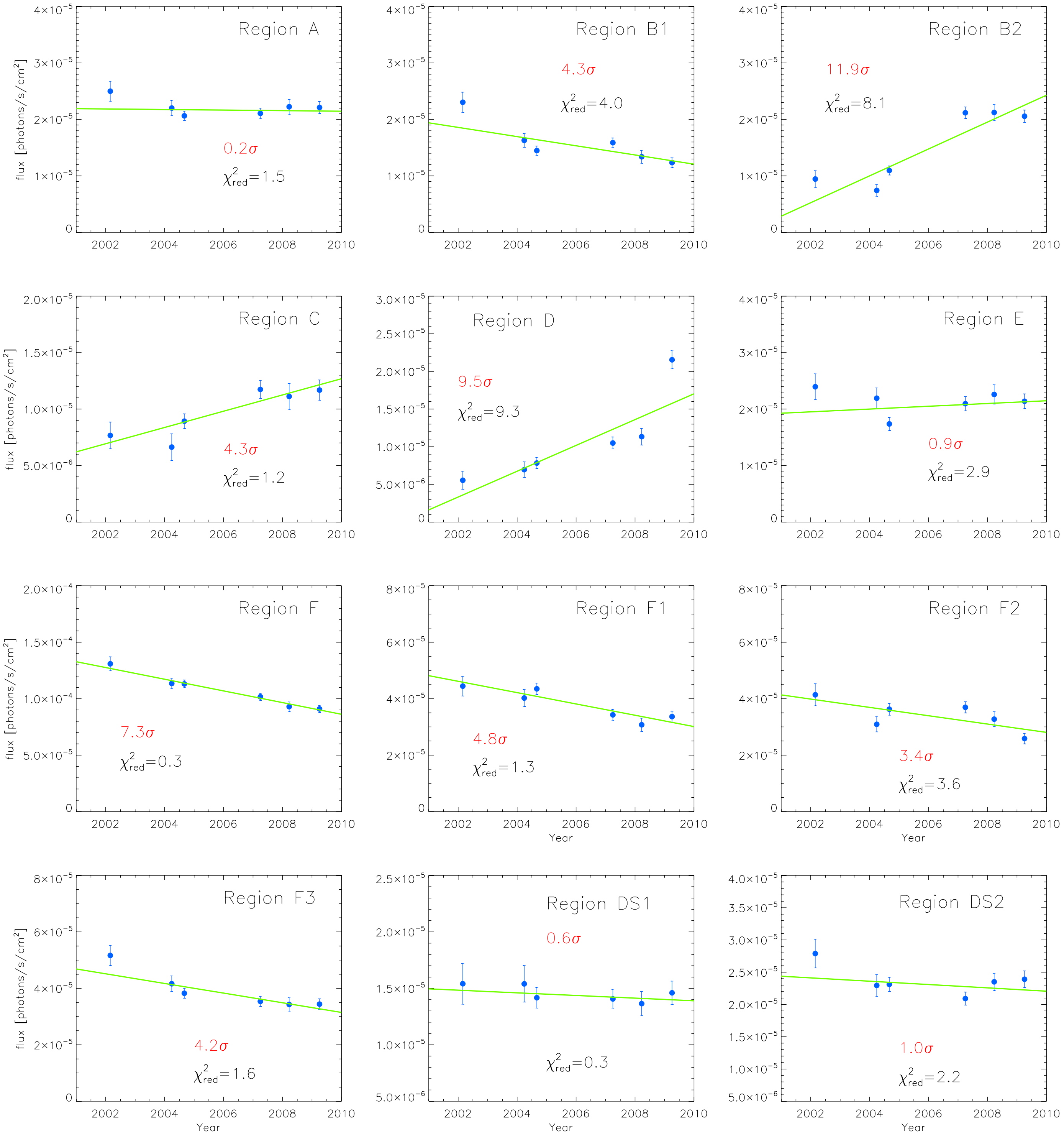

Fig. 4. Lightcurves of the Fe-Kα flux from the filaments in the GC. The flux is plotted in units of 10^{-5} photons cm^{-2} s^{-1}. The green line represents the best fit linear function to the data, whose parameters are reported in Table 4. In each panel we present the significance of the measured gradient (B/σ_B) together with the $\chi^2_{\rm red}$ for the best fit linear function.

curves although, as for region E, we found some little excursions in the lightcurve of the region DS2.

To summarize, we have independently established a pattern of Fe-Kα variability similar to what already found by Ponti et al. (2010) for the clouds A, B2, D, E and F. For cloud B1, our analysis implies a decrease of the line flux at a confidence level of 2.6σ, whereas Ponti et al. (2010) report a constant line flux for this cloud (designated MC2 in their study); we attribute this significant difference to the use of the background modelling. This result has implications for the location of the cloud relative to the leading and trailing edges of the ionizing wavefront. We have also studied three lower-surface brightness regions (C, DS1 and DS2), the first of which shows an interesting step-wise increase in its fluorescent line flux, with the latter two having constant light curves.

Table 4. Results for the study of the Fe-Kα variability in the selected regions and sub-regions.

Region	B (10^{-6})	σ_B (10^{-6})	$\#_\sigma$ (B/σ_B)	$\chi^2_{\rm red}$
A	–0.05	0.21	0.2	1.5
B1	–0.81	0.19	4.3	4.0
B2	2.38	0.20	11.9	8.1
C	0.72	0.17	4.3	1.2
D	1.71	0.18	9.5	9.3
E	0.25	0.27	0.9	2.9
F	–5.18	0.71	7.3	0.3
F1	–2.00	0.42	4.8	1.3
F2	–1.48	0.43	3.4	3.6
F3	–1.71	0.41	4.2	1.6
DS1	–0.12	0.21	0.6	0.3
DS2	–0.26	0.26	1.0	2.2

Notes. The second and third columns give the value of the gradient obtained for the best-fit linear function together with its uncertainty (in units of 10^{-6} photons cm^{-2} s^{-1} year^{-1}). The fourth and the fifth columns report, respectively, the number of sigma for the deviation from the constant behaviour of the best-fit function and the reduced χ^2 for the linear fit.

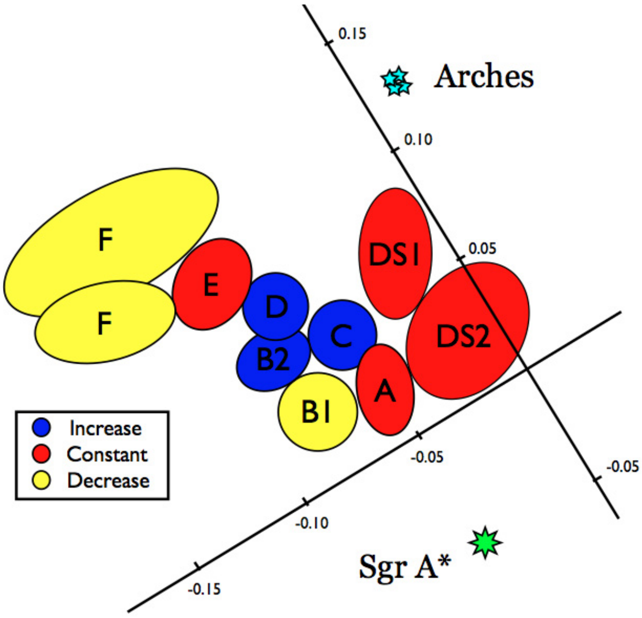

Fig. 5. Colour-coded sketch of the molecular clouds and Fe-Kα line flux variability studied in this work. The circles and ellipses represent the regions selected for the timing and spectral studies (see also the right panel of Fig. 2). The colours are blue (increase of the 6.4-keV line flux), red (constant) and yellow (decrease). A Galactic coordinate grid, and the positions of Sgr A* (green star) and the Arches cluster (cyan stars) are also indicated.

In order to investigate the spatial dependency of the observed Fe-Kα variability, and show the complexity of its pattern across the inner CMZ, we sketched the distribution of the MCs studied in this paper, with a colour-coding which identifies the type of variability measured in the 6.4-keV line flux (see Fig. 5). The most noticeable increase in the Fe-Kα flux comes from the zone bounded by $0.05° < l < 0.1°$ and $-0.1° < b < -0.05°$ (l and b are, respectively, galactic longitude and latitude), which encompasses the regions B2 and D. Indeed, these molecular filaments show the clearest evidence for Fe-Kα variability across the selected regions. Besides these complexes, region C also shows an upwards trend in its Fe-Kα surface brightness, whereas the G0.11-0.11 cloud shows fading 6.4-keV line emission. Ponti et al. (2010) have suggested that this complex pattern of variability can be largely explained in terms of a single flare from Sgr A* illuminating molecular clouds at differing positions along the line of sight. However, as we show below, detailed consideration of the spectral properties of the various MCs lead us to conclude that this is not the complete story.

3.3. *Spectroscopy: looking for the reflection imprints*

3.3.1. Method

In order to study the spectral features typical of an XRN, we have considered the spectra from the PN camera of the regions highlighted in Fig. 5 (see also Table 2). For this analysis we selected only PN spectra because of the much higher effective area in the hard X-ray band ($\gtrsim$6 keV). To build the PN spectra for the Fe-Kα bright filaments, we used the same GTI filtered event files as employed to construct the fluence map in Sect. 2. We stacked all the spectra (of both the source and the background) and the response files using the ftools MATHPHA, ADDARF and ADDRMF, neglecting the 6.4-keV line variability. The background region was centred on RA = 17:45:42.289, Dec = –29:07:53.39 (circle 1 arcmin in radius, see left panel of Fig. 2), at the same Galactic latitude as the filaments in order to avoid any systematics due to the different intensity of the Galactic ridge emission at different Galactic latitudes.

The spectral model used in the fitting comprises two thermal plasmas (APEC, Smith et al. 2001) with a metallicity fixed at 2 times solar (e.g., Nobukawa et al. 2010), two gaussian emission lines (GAUSS) which account for the Fe-Kα and Kβ lines (the ratio of the line fluxes has been fixed to 0.11, Koyama et al. 2009), and a non-thermal power-law continuum (POW), with a slope fixed at $\Gamma = 1.9$. The latter is the spectral index obtained from a joint fit of the stacked PN spectra of all the MCs using the model defined below (where we assume that primary illumination source is the same for all the XRN); specifically the best-fit value was $\Gamma = 1.9^{+0.1}_{-0.2}$. All the previously listed components are then subject to a common photoelectric absorption by the line-of-sight column density, $N_{\rm H}$ (WABS$_1$, Morrison & McCammon 1983).

We model the absorption within the MCs in terms of an intrinsic column density $N_{\rm H_C}$ (WABS$_2$) plus an additional contribution to the optical depth of the Fe-K absorption edge at 7.1 keV. The latter allows the iron abundance relative to the solar value ($Z_{\rm Fe}$) in the MC to be greater than 1 (since the WABS prescription assumes solar metal abundances). In our spectra model the extra optical depth τ (the free parameter in EDGE, see below) and $N_{\rm H_C}$ are tied by the relation:

$$\tau = (Z_{\rm Fe} - 1) \times \sigma_{\rm Fe} \times A_{\rm Fe:H} \times N_{\rm H_C} = \frac{N_{\rm H_C}}{10^{22}} \times (Z_{\rm Fe} - 1) \times 0.0116,$$

where $A_{\rm Fe:H} = 3.3 \times 10^{-5}$ is the (solar abundance) ratio of Fe to H atoms and $\sigma_{\rm Fe} = 3.5 \times 10^{-20}$ cm^2 is the photoionisation cross-section of the Fe-K shell.

In the event we fixed $Z_{\rm Fe}$ at a value of 1.6 (a choice which will be justified in Sect. 4.1). Note that $N_{\rm H_C}$ (and τ) account for the absorption imprinted on the reflected continuum by the MC both up to and after the point of scattering. A simple simulation shows that, to zeroth order, the value of $N_{\rm H_C}$ so determined is comparable to the total column density through the cloud

Table 5. Results from the analysis of the PN time-averaged spectra of the Fe-Kα bright filaments.

	A	B1	B2	C	D	E	F	DS1	DS2
N_H	$7.0^{+0.6}_{-0.4}$	8.0 ± 0.4	$8.1^{+0.4}_{-0.5}$	8.0 ± 0.5	6.8 ± 0.5	$6.7^{+0.2}_{-0.3}$	7.8 ± 0.3	8.0 ± 0.6	$7.1^{+0.7}_{-0.6}$
$kT_{\rm warm}$	0.9 ± 0.1	0.9 ± 0.1	$0.89^{+0.04}_{-0.07}$	$0.79^{+0.04}_{-0.06}$	1.0 ± 0.1	$1.01^{+0.05}_{-0.03}$	$1.08^{+0.01}_{-0.03}$	0.7 ± 0.1	0.7 ± 0.1
norm	$3.5^{+1.6}_{-0.6}$	$5.5^{+0.9}_{-0.8}$	$4.4^{+1.1}_{-0.8}$	$5.4^{+1.6}_{-1.3}$	$2.7^{0.6}_{-0.5}$	$4.7^{+0.7}_{-0.5}$	$24.5^{+2.5}_{-1.9}$	$6.4^{+3.0}_{-1.8}$	$6.5^{+4.7}_{-1.8}$
$kT_{\rm hot}$	8.9 ± 1.2	6.5 fix	$5.3^{+1.8}_{-1.9}$	6.5 fix	6.5 fix	6.5 fix	–	$7.4^{+1.2}_{-1.4}$	$7.5^{+0.8}_{-1.0}$
norm	$3.1^{+0.5}_{-0.4}$	2.0 ± 0.3	1.1 ± 0.3	1.4 ± 0.3	0.6 ± 0.3	$0.8^{+0.3}_{-0.2}$	–	3.3 ± 0.6	6.1 ± 0.7
N_{H_C}	$18.4^{+1.5}_{-2.7}$	$10.2^{+2.3}_{-2.0}$	$12.3^{+3.0}_{-2.7}$	$5.8^{+2.3}_{-1.9}$	$13.2^{+5.0}_{-4.7}$	$9.6^{+1.7}_{-1.4}$	$9.2^{+2.7}_{-2.3}$	$15.5^{+3.9}_{-3.3}$	14.5 ± 2.3
E_{64}	$6.420^{+0.007}_{-0.004}$	$6.416^{+0.007}_{-0.006}$	$6.415^{+0.003}_{-0.004}$	$6.421^{+0.006}_{-0.013}$	$6.417^{+0.011}_{-0.007}$	6.417 ± 0.008	6.411 ± 0.005	$6.414^{+0.010}_{-0.009}$	6.412 ± 0.007
σ	0.03 ± 0.01	0.05 ± 0.01	$0.039^{+0.005}_{-0.008}$	$0.042^{+0.015}_{-0.011}$	$0.043^{+0.012}_{-0.020}$	$0.030^{+0.018}_{-0.014}$	$0.029^{+0.009}_{-0.012}$	$0.041^{+0.014}_{-0.019}$	$0.053^{+0.009}_{-0.012}$
F_{64}	2.5 ± 0.1	1.7 ± 0.1	2.0 ± 0.1	1.1 ± 0.1	1.1 ± 0.1	2.0 ± 0.1	$9.1^{+0.3}_{-0.5}$	1.5 ± 0.1	2.6 ± 0.1
EW	0.9 ± 0.1	0.9 ± 0.1	$1.5^{+0.3}_{-0.2}$	$1.0^{+0.2}_{-0.1}$	$1.3^{+0.4}_{-0.3}$	1.4 ± 0.2	1.7 ± 0.2	0.9 ± 0.2	0.9 ± 0.1
τ	0.13	0.07	0.08	0.04	0.09	0.07	0.06	0.11	0.10
$\rm norm_{pow}$	$9.3^{+0.7}_{-0.6}$	$6.2^{+0.5}_{-0.4}$	$4.4^{+0.5}_{-0.4}$	3.7 ± 0.3	$2.8^{+0.5}_{-0.4}$	$5.0^{+0.6}_{-0.2}$	$18.7^{+1.6}_{-1.3}$	6.0 ± 0.8	$10.5^{+0.9}_{-0.8}$
chi^2/d.o.f.	521.62/1283	546.36/1316	403.12/1246	432.87/1215	364.12/1130	473.89/1254	588.24/1551	477.09/1336	596.67/1503
C-stat/d.o.f.	1612/1529	1654/1526	1521/1529	1649/1529	1644/1530	1654/1528	1718/1530	1571/1527	1548/1528

Notes. The spectral parameters reported are the column density along the line of sight (N_H, in units of 10^{22} cm^{-2}), the temperatures (in keV) of the warm and the hot plasma components and their normalisations (in units of 10^{-17} and $10^{-18} \int n_e n_H dV/4\pi D^2$ respectively), the column densities intrinsic to the MCs (N_{H_C} in units of 10^{22} cm^{-2}), the central energy and the intrinsic width σ of the Fe-Kα line (in keV), the 6.4-keV line flux (in units of 10^{-5} photons cm^{-2} s^{-1}), the EW of the 6.4-keV line (in keV), the excess optical depth τ at the Fe-K edge, the power law normalisation (in units of 10^{-4} photons cm^2 s^{-1} keV^{-1} at 1 keV) and the C-stat value and the degree of freedom for the best fit model.

(although, of course, the exact relation will depend on the geometry). To summarize, the model used in the spectral analysis of the clouds is (in XSPEC format):

$$\mathrm{WABS_1} * [\mathrm{APEC} + \mathrm{APEC} + \mathrm{WABS_2} * (\mathrm{GAUSS} + \mathrm{GAUSS} + EDGE * POW)].$$

In the spectral fitting procedure we ignored the channels encompassing the Cu-Kα line (7.8–8.2 keV) in order to minimize the effects of the instrumental background on the modelling of the reflection component. Also, we again employed the Cash statistic because of the low signal-to-noise ratio in the spectral channels and because its use gave tighter contraints on the derived parameter values.

In region F the normalization of the hot thermal component was compatible with being zero and therefore we excluded this component from the best-fit model. Also, in fitting the spectra from regions B1, C, D and E, we were forced to fix the temperature of the hot component to $kT = 6.5$ keV (Koyama et al. 2007) in order to make the fit converge (see Table 5). Although we have applied the background subtraction technique in this study, all the spectra still exhibit strong residual contributions from the two APEC components (as is evident in Fig. 6).

The specific goal of this analysis was to quantify the intrinsic column density (N_{H_C}) of the MCs and also to establish the equivalent width (EW) of the 6.4-keV line with respect to the underlying ionising continuum. These important parameters will be of use in Sects. 4 and 5.

3.3.2. Results

Sunyaev & Churazov (1998) have shown that in the XRN model, the 6.4-keV line emission has to be accompanied by strong absorption above 7.1 keV, the minimum energy that a photon must have in order to be able to produce a K-shell vacancy in neutral Fe via the photoelectric effect. Moreover, because the primary source of ionisation is not seen directly by the observer, the EW of the line is expected to be very high, i.e. $\gtrsim$1 keV. On the other hand, the depth of the Fe absorption edge at 7.1 keV is strongly related to the intrinsic column density of the MC, with columns in excess of 10^{23} cm^{-2} resulting in the imprinting of very strong Fe-K edge features on the emergent (i.e., electron-scattered) continuum. In Fig. 6 and Table 5, we present the results of our search for the imprints of reflection on the time averaged spectra of the selected GC molecular filaments. We measure a high value for the EW of the 6.4-keV line in all the MCs studied. Interestingly the largest EWs (~1.5 keV) were those of the B2 and F clouds, both of which exhibit pronounced Fe-Kα flux variability (a decreasing flux in the case of the F cloud and an increasing flux for B2). Another very interesting finding is that the values of N_{H_C} typically lie in the range 6 to 20×10^{22} cm^{-2}, which is significantly higher than previous estimates/assumptions for these clouds (e.g. Ponti et al. 2010).

A very important result of our work is the identification of the hard non-thermal component associated with the 6.4-keV line, which in the XRN model represents the fraction of the incident continuum Thomson scattered by the molecular material. In all the observed spectra we were able to discern an underlying hard continuum, which via a joint-fit to all the MC spectra, was modelled as a power-law with a photon index $\Gamma \approx 1.9$. This value is very typical of the continuum slopes that characterise the spectra of luminous AGN.

We have also investigated the characteristics of the Fe-Kα line, in terms of its energy and width. For this purpose we built a time-averaged spectrum for the whole region, stacking all the spectra across all the observations. In this stacked spectrum, the intrinsic width of the line is 36 ± 3 eV, while its peak is at 6414 ± 2 eV, slightly higher than the nominal value of 6403 eV for neutral iron[1]. The results from the individual spectra (see Table 5) show the same trend, with the measured Fe-Kα line energy in all cases exceeding the theoretical value. Although the EPIC calibration is known to be better than 10 eV, the presence of soft protons in the FOV might slightly change

---

[1] The nominal values for the energy peak of the Fe-Kα and Cu Kα lines have been taken from `http://physics.nist.gov`.

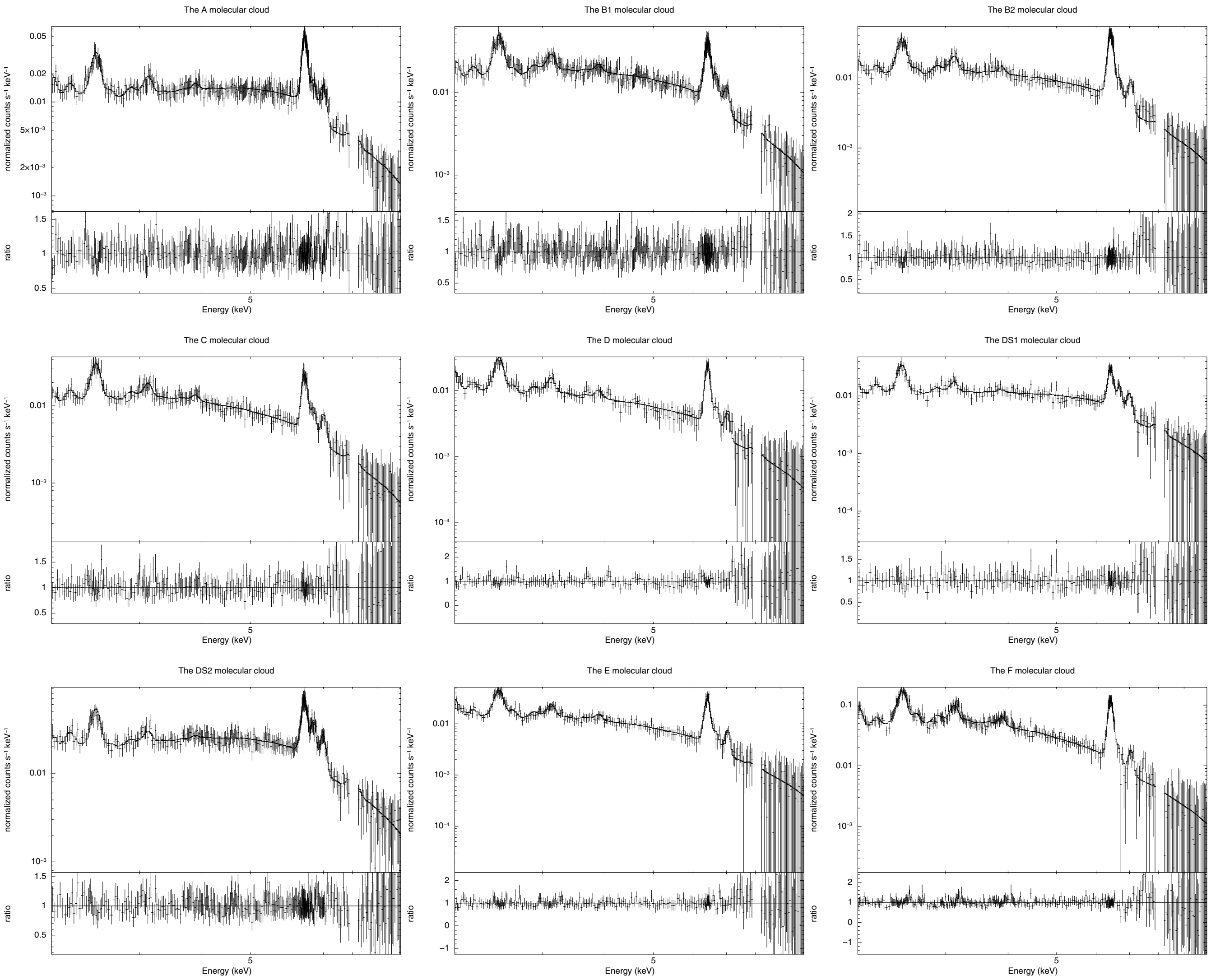
The A molecular cloud

The B1 molecular cloud

The B2 molecular cloud

The C molecular cloud

The D molecular cloud

The DS1 molecular cloud

The DS2 molecular cloud

The E molecular cloud

The F molecular cloud

Fig. 6. Time-averaged PN spectra of the set of MCs in the present study. Each panel shows the measured data along with the best fitting spectral model and (in the lower section) the ratio of these two quantities. The spectral channels encompassing the Cu-Kα line at 8.05 keV (7.8–8.2 keV) have been excluded from the fitting.

the energy and the width of the lines (Ponti et al. 2010). To check whether these are instrumental effects or real features, we measured the same quantities for the Cu instrumental line at 8.05 keV (before cutting it out). The centroid of the Cu Kα line is at 8047^{+4}_{-2} eV, while its width is 34^{+6}_{-4} eV. The line peak is in good agreement with its nominal value of 8048 eV. Although a relative shifting between the two lines is present (the Cu Kα peak perfectly matches the theoretical expectation, whereas the Fe-Kα is noticeably higher), taking into account the systematics and the statistical uncertainties, we conclude that no statistically significant line blueshift and broadening has been measured and that our results are consistent with emission from neutral, or close-to-neutral, Fe atoms embedded in the material of the cold molecular clouds. The 11 eV upwards shift of the Fe-Kα line central energy might be the result of very modest ionisation of the Fe atoms (Fe II to FeX); in fact, the ionisation potentials for the low ionisation Fe atoms are between few 10 eV and few 100 eV, which suggests that these ionisation states of Fe might plausibly exist in GC MCs, given the peculiar environment. We also note that *Suzaku* measured the Fe-Kα line energy in the molecular filaments to be 6409 ± 1 eV with a line width of 33^{+2}_{-4} eV, the latter being marginally higher than the expected systematics (≈30 eV) (Koyama et al. 2007).

The results of this spectral analysis will be used in Sects. 4 and 5 in order to derive a geometrical distribution of these nebulae in the GC region and a X-ray lightcurve for the putative energising source.

4. The derived properties of the MCs

4.1. Relative Fe abundance in the clouds

In this Section we make use of the measurements of the EW of the Fe-Kα line from the spectral analysis of the stacked PN spectra (see Table 5) to infer the mean Fe abundance across the MCs which compose our sample. The underlying assumption in this section is that the Fe fluorescence arises as a result of the X-ray illumination of the clouds by one or more X-ray outbursts in Sgr A*. To proceed we first require an expression for Fe-line equivalent width, in terms of the intensity of the X-ray illumination and the cloud properties. As discussed in Sunyaev & Churazov (1998), the Fe-Kα line flux (F_{64}) emanating from the illuminated cloud can be written as:

$$F_{64} \approx \frac{\Omega}{4\pi D^2}\, Z_{\rm Fe}\, \tau_{\rm T}\, I_8 \quad \text{photons cm}^{-2}\ \text{s}^{-1}, \tag{1}$$

in this equation Ω is the solid angle (in units of 4π) subtended by the diffuse cloud from the perspective of the radiation source, D is the distance to the GC, $Z_{\rm Fe}$ is the Fe abundance relative to solar within the MC, $\tau_{\rm T}$ is the optical depth due to Thomson-scattering through the cloud and I_8 is the photon flux from the source at 8 keV (in units of photon $\rm s^{-1}\ keV^{-1}$).

In addition the scattered continuum at 6.4 keV measured at an angle θ with respect to the direction of travel of the incident radiation is:

$$S_{64} = \frac{\Omega}{4\pi D^2}\,\tau_{\rm T}\,\left(1+\cos^2(\theta)\right)\,I_8\;1.172\;\;\text{photons cm}^{-2}\,\text{s}^{-1}\,\text{keV}^{-1}, \tag{2}$$

we can therefore write the EW of the Fe-Kα line with respect to the reflected continuum as:

$$EW \approx \frac{850\,Z_{\rm Fe}}{[(1+\cos^2(\theta)]}\;\text{eV}. \tag{3}$$

In these calculations we assume that the cloud is not optically thick along any viewing direction. We also assume the photon index of the incident radiation is $\Gamma_{\rm in}\approx 2$; the impact of using $\Gamma_{\rm in} = 1.5$ is to increase the EW estimate by ~20%.

If we make the assumption that $Z_{\rm Fe}$ is constant across the MCs considered in this study, then we can use Eq. (3) to determine the value of this parameter. For this purpose we need to make a geometrical assumption, namely that the clouds are distributed such as to give a reasonably uniform distribution of scattering angles within the range $25^\circ \lesssim \theta \lesssim 155^\circ$. This is equivalent to assuming the distance of each cloud along the line of sight, measured relative to the plane of Sgr A*, is less than twice its projected distance from Sgr A*. On this basis, we obtain $\langle 1+\cos^2(\theta)\rangle = 1.33$. The mean Fe-K$\alpha$ EW based on the measurements for the nine clouds reported in Table 5 is 1.0 ± 0.1 keV, where we have given each measurement a weight proportional to the inverse of the error squared. Substituting this weighted mean for the EW and the value for $\langle 1+\cos^2(\theta)\rangle$ noted above into Eq. (3), we obtain an estimate for the relative abundance of Fe in the clouds of $Z_{\rm Fe} = 1.6\pm0.1\,Z_\odot$. Note that if we relax the geometrical constraint to allow the clouds to be displaced along the line of sight relative to the plane of Sgr A* by up to three times their projected distance, then the relative abundance estimate increases by less than 5%. This important result confirms a higher than solar metallicity for the MCs and presumably the interstellar medium generally in the GC region.

The geometry of the illumination process is shown in Fig. 7, which also defines the distance along the line of sight behind (or in front) the plane of Sgr A* ($d_{\rm los}$) and the distance of the cloud as projected in the sky ($d_{\rm proj}$), as employed in our work. In Fig. 7, two clouds are shown at the two angles θ and 180-θ for which the scattering effects are the same. Troughout our work, we will always consider a positive $d_{\rm los}$ term for the 180-θ case, and negative otherwise.

Another interesting application of Eq. (3) deals with the geometry of the illumination process. In principle, if the Fe abundance is tightly constrained, then the accurate measurement of the EW of an individual cloud will allow the scattering angle θ to be determined and hence the cloud's position in 3-dimensional space to be inferred (albeit with an ambiguity as to whether the cloud is positioned in front of or behind the plane of Sgr A*). The process is illustrated in the left panel of Fig. 8, which shows how the inferred relative abundance $Z_{\rm Fe}$ varies as a function of the scattering angle θ for the set of clouds in our sample. The intersection of the horizontal line (corresponding to $Z_{\rm Fe} = 1.6$) with the plotted curve for a particular cloud determines the scattering angle for that cloud (with the positional ambiguity arising from the fact that the scattering angle can be θ or $180^\circ - \theta$). Although there is no such intersection for B2 and F clouds, when the errors on the EW measurements (which are not shown in Fig. 8) are taken into we can also derive a range of possible angles for these two clouds. The error range on all the scattering determinations for all the other clouds can similarly be determined.

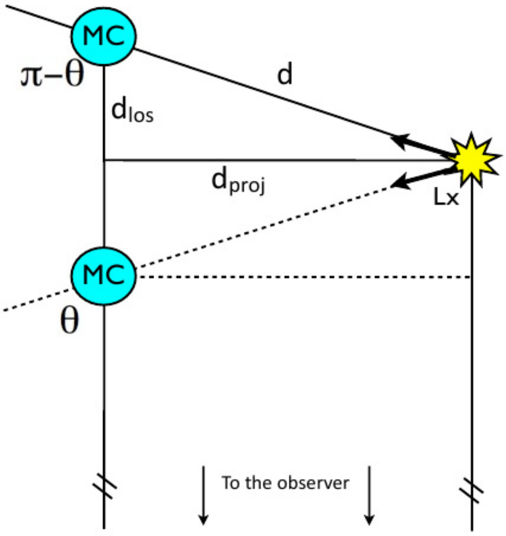

Fig. 7. The cloud-source geometry for the two cloud positions ($\theta, \pi-\theta$) which produce the same effective scattering. The total distance from the cloud to the source (d), the projected distance on the plane of the sky ($d_{\rm proj}$), and the line of sight displacement with respect to the Sgr A* plane ($d_{\rm los}$) are all indicated, as are the scattering angles θ and $\pi-\theta$.

The results of the above analysis are plotted in the right panel in Fig. 8. This figure shows for each MC the line-of-sight displacement relative to the plane of Sgr A* versus the projected distance from Sgr A* (on the plane of the sky) as determined from the scattering angle constraints. In the figure, the MCs are positioned behind the plane of Sgr A* but in fact the method cannot distinguish whether cloud is in front of or behind this plane (see above). Figure 8 also shows that our analysis is self-consistent in the sense that the geometrical assumption employed when calculating the averaged Fe abundance across the set of clouds holds true (i.e., all the MCs lie in the region bounded by the plane of Sgr A* and the straight line $d_{\rm los} \leq 2\times d_{\rm proj}$). Unfortunately, given the current EW measurement errors, the scattering angle determinations results in only weak constraints on the locations of a few of the clouds.

In all of these calculations, we have assumed that the MCs are illuminated by the same powerful X-ray source, in a pure XRN scenario. Clearly if there is a significant contribution to the Fe-Kα line from an alternative process, such as CR bombardment, then this would impact on these results. However we show in Sect. 6 that at least for brightest Fe-line emitting clouds, X-ray illumination is the most likely excitation source of Fe fluorescence. Potentially, the method outlined above provides a powerful tool for the investigation of the illumination geometry of XRN, particularly when coupled with studies at radio and other wavelengths which may serve to resolve the ambiguity in the derived geometry.

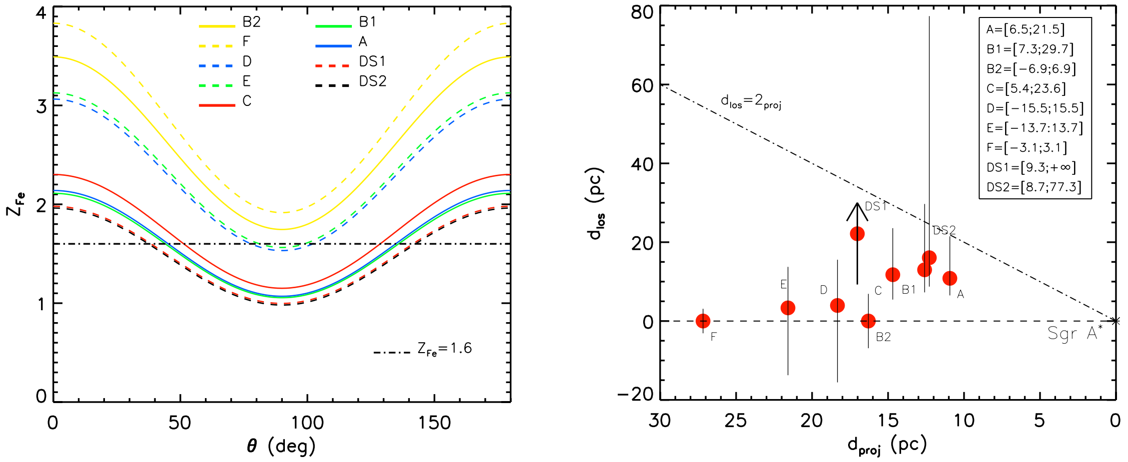

Fig. 8. *Left panel*: relative Fe abundance Z_{Fe} as a function of the scattering angle θ for the different MCs obtained by using the measured EW and Eq. (3). The horizontal dashed-dotted line represents the average metallicity ($Z_{Fe} = 1.6$) inferred for set of MCs. *Right panel*: line-of-sight displacement plotted against the projected distance d_{proj} for each MC. The d_{los} value for the DS1 cloud is a lower limit ($d_{los} \geq 9.3$ pc). The horizontal dashed line represents the plane of Sgr A* at $d_{los} = 0$. The dashed-dotted line shows the line $d_{proj} = 2 \times d_{los}$. We make the assumption that the clouds are located in the region between the dashed and dashed-dotted lines (see text). The permitted d_{los} range (in pc) for each cloud is given in the top-right box. Note: the method does not distinguish between whether an individual cloud lies in front or behind the plane of Sgr A* (i.e., at +ve or –ve d_{los}).

4.2. Column densities of the clouds

In the XRN scenario, both the column density of Fe atoms within the cloud and the distance of the cloud from the illuminating source are the crucial parameters, when estimating the X-ray luminosity required to produce a given Fe-Kα flux. Previous studies have often determined the former using estimates of the hydrogen column density for the cloud, N_{H_C}, combined with the solar Fe:H ratio and an assumed value for Z_{Fe}. In turn, the estimates of N_{H_C} have often been inferred from intensity maps of CO, CS or other molecular tracers of high density material in the inner Galaxy. However, the estimation of the cloud N_{H_C} from molecular line observations is notoriously difficult with different measurement techniques often giving different results. For example, the G0.11-0.11 cloud (our region F) has been the subject of numerous studies over the last decade. Using, respectively, the intensity of the CS and the $H^{13}CO^{+}$ emission lines, Amo-Baladrón et al. (2009) and Handa et al. (2006) measured two extreme values for the N_{H_C} of this MC, namely 2×10^{22} and 10^{24} cm^{-2}, respectively.

A better approach is to measure the column density of Fe atoms in the cloud directly from the X-ray spectrum. This is essentially the approach we have taken in the spectral fitting reported in Sect. 3.3, where the Fe column density can be obtained from the quoted N_{H_C} values as:

$$N_{Fe} = N_{H_C} \times A_{Fe:H} \times (Z_{Fe}) = N_{H_C} \times 5.3 \times 10^{-5} \quad \mathrm{cm}^{-2}.$$

In practice, the fact that we were able to set $Z_{Fe} = 1.6$ and the spectral index of the underlying power-law continuum (arising from reflection) to $\Gamma = 1.9$, resulted in a reasonable robust set of N_{H_C} measurements.

The N_{H_C} values we derived for our set of 9 clouds are summarised in Table 6, where a comparison is made with the earlier estimates (based on radio molecular line measurements) by Ponti et al. (2010) for the same MC sample. Clearly the X-ray measurements lead to substantially higher estimates of the cloud column densities, more similar to the values measured within the Sgr B2 complex by Nobukawa et al. (2011). This in turn has a significant impact on the inferred geometry and time delays within the cloud system (see below). To conclude, we note that the XRN parameters we have found for the MCs within 30 pc of Sgr A* are in good agreement with the ones for the Sgr B2 MC found by Nobukawa et al. (2011), i.e. $Z_{Fe} = 1.3 \pm 0.3\ Z_{\odot}$ and $\Gamma = 2.5 \pm 0.6$.

Table 6. Comparison between the cloud density measurements.

A	B1	B2	C	D	E	F	DS1	DS2
4.0	≤2.0	9.0	–	9.0	9.0	2.0	–	–
18.4	10.2	12.3	5.8	13.2	9.6	9.2	15.5	14.5

Notes. The first line reports the N_{H_C} values employed by Ponti et al. (2010), whereas the second lists the results from this paper (see Table 5). All values are in units of 10^{22} cm^{-2}.

5. The X-ray lightcurve of Sgr A* over the last 200 years

5.1. Placing constraints on the lightcurve of Sgr A*

If the number of Fe atoms in a particular MC is known, it is possible to use the observed Fe-Kα flux to estimate the cloud's position relative to the illumination source, assuming that the cloud remains optically thin at the line energy. This method has been recently employed by Ponti et al. (2010), who assumed that the MCs in their study are all illuminated by a past outburst on Sgr A* reaching an X-ray luminosity of $\sim 10^{39}$ erg s^{-1}. However, in the previous section (Sect. 4.2) we noted that the N_{H_C} values used by these authors may be severe underestimates, implying the need for a substantial revision of the cloud-source geometry.

Following the same approach as discussed by Sunyaev & Churazov (1998), Eq. (1) can be used to derive an expression for the separation, d, of the MC from the ionising source as:

$$d^2 = \frac{10^7\, L_X\, \tau_T\, R^2\, Z_{Fe}}{16\pi\, D^2\, F_{64}}. \tag{4}$$

In this formula τ_T is the optical depth of the MC to Thomson scattering and R is the radius of the cloud. The other parameters are the X-ray luminosity L_X of the source (in a nominal 2−10 keV bandwidth), the relative Fe abundance Z_{Fe} within the cloud, the distance to the GC D and the measured Fe-Kα line flux F_{64}. In applying this formula we make the assumption that the cloud is sufficiently symmetric such that we can employ the values of τ_T and R determined by observation along our particular line of sight.

If we assume that the clouds are illuminated by a past outburst on Sgr A* with $L_X = 1.4 \times 10^{39}$ erg s^{-1} (e.g. Ponti et al. 2010) then we can use Eq. (4) to calculate the d for each of our 9 clouds, since we already know all the other quantities. Once the value of d is derived, we can determine the line of sight displacement $d_{\rm los}$ of each cloud by using the projected separation from Sgr A* $d_{\rm proj}$ on the plane of the sky (see Table 2). Again there is an ambiguity as to whether the cloud resides in front of or behind the plane containing Sgr A*. Employing this method we find that the spread along the line of sight of the MCs is almost an order of magnitude larger than the spread in the projected distances. Moreover, the inferred line of sight distribution of the MCs is incompatible with the 3D distribution we derived from the EW relation in Sect. 4.1. The implication is that we must tune (i.e. reduce) the luminosity of the ionizing source to match the observed Fe-Kα characteristics of the clouds.

Ideally, rather than assuming a particular L_X for the outburst, we should build a model for the X-ray activity of Sgr A* over the last few hundreds years, which accounts for all the Fe-Kα variations measured in the MCs in our sample. Unfortunately the uncertainty in the position of the clouds along our line of sight (relative to the plane containing Sgr A*) hampers this endeavour. In the general case, when employing a geometrical model such as the one shown in Fig. 7, the luminosity of the outburst is given as:

$$L_X = 2.9 \times 10^{39} \left[\frac{F_{64}\,(d_{\rm proj}/\sin(\theta))^2}{R^2\,\tau_T\,Z_{\rm Fe}} \right] \text{erg s}^{-1}, \qquad (5)$$

also, the delay of the reflected signal relative to the direct light from Sgr A* is:

$$\Delta t = \frac{1}{c}\,d_{\rm proj} \left[\sqrt{1 + \cot^2\theta} - \cot\theta \right] \text{s}. \qquad (6)$$

By allowing θ to vary over a particular range, one can use the above equations to produce the track of L_X versus Δt matching the Fe-Kα line emission and other properties of the particular cloud. Figure 9 shows the result of this analysis, where θ was constrained to vary within the interval 25°−155° as in Sect. 4.1.

However, we can also use the results from Sect. 4.1 which are summarised in the right-hand panel of Fig. 8 to add the further constraints in Fig. 9, represented by the vertical lines.

In Fig. 9 we have split the clouds into subgroups depending on whether they exhibit a decreasing flux (clouds B1 and F, top panel), an increasing flux (clouds B2, C and D, middle panel) or a constant level (clouds A, E, DS1 and DS2, bottom panel). In each of the three panels the different colours refer to different clouds with the upper and lower limit ranges on L_X shown by the thinner curves of the same colour. Note that in deriving these plots we use the Fe-Kα fluxes from the analysis of the stacked PN spectra (i.e., the plots are based on the average Fe-Kα flux of the cloud).

The challenge is to see whether there is a restricted pattern of variability in Sgr A*, which plausibly matches all of the constraints implied by Fig. 9. Specifically we are interested in those L_X-delay combinations within each of sub-groups, which provide a consistent description of the Sgr A* variability (i.e., where the L_X values for the different clouds within a particular delay range are compatible with each other). Of course, given the limitations we should bear in mind that there can be no guarantee that any particular solution is unique.

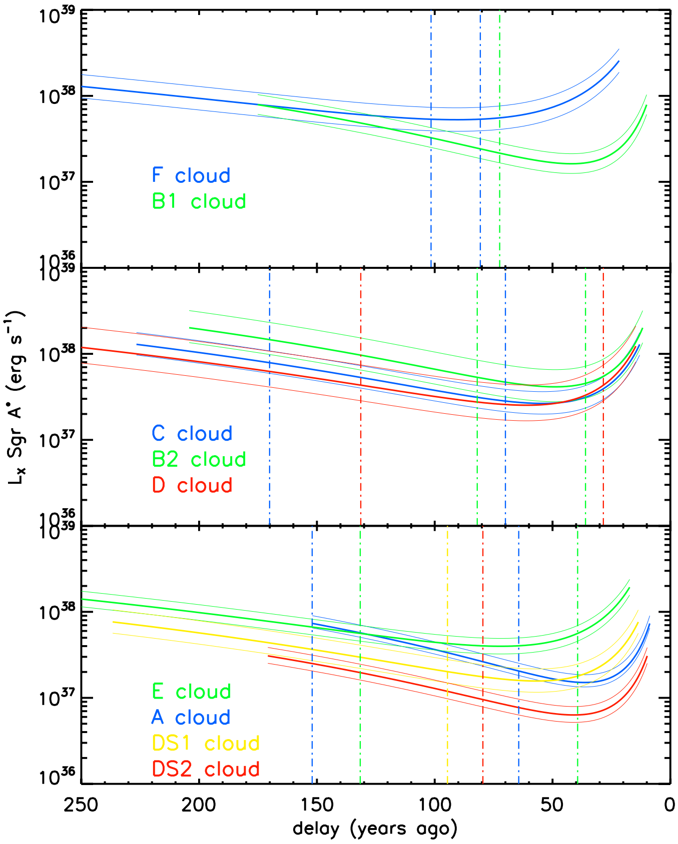

Fig. 9. X-ray luminosity as a function of the time delay for the different MCs, as inferred from the measured cloud properties. We have divided the MCs into subgroups depending on the type of Fe-Kα line variability exhibited. Also plotted are the 90% confidence ranges on the L_X calculation. The vertical dotted lines represent the constraints on θ derived in Sect. 4.1. Where only one vertical line is shown for a cloud, it represents the right-hand boundary of the allowed range; in these cases the second boundary is situated to the left of the Y axis (i.e., $\theta \geq 155$ deg), and therefore not plotted.

The B1 and F clouds: in the top panel of Fig. 9 we can see that the L_X curves for the B1 and F clouds show a reasonable match around an X-ray luminosity of $\sim 4 \times 10^{37}$ erg s^{-1} and a time delay around ∼100 years. If these clouds are responding to the same decrease in the incident L_X, then we might infer that the scattering angle for the cloud F is ∼95° and that of the cloud B1 near to 135°. This places the cloud F roughly on the same plane as Sgr A* and the cloud B1 15 pc *behind it* (i.e. note that this approach can in principle resolve the positional ambiguity alluded to earlier). For both clouds the measured excursion of the Fe-Kα flux in their lightcurves is about factor of two, implying a commensurate decline in the L_X of Sgr A* over 7 years. As shown in Fig. 9, the geometry inferred for these two MCs agrees remarkably well with the results obtained earlier (see Sect. 4.1).

In conclusion, a drop in the X-ray luminosity of Sgr A* by a factor of two, from ~ 4–2×10^{37} erg s^{-1} around 100 years ago may explain the decaying Fe-Kα line flux currently observed from the B1 and F clouds.

The B2, C and D clouds: in the same way we can try to put together a scenario which explains the steady increase in the Fe-Kα flux observed from clouds B2, C and D clouds. (middle panel of Fig. 9). Here the situation is more complex, since the tracks for the three clouds cluster together in a fairly tight fashion along a broad extent of the time axis. In order to restrict the possibilities we need to bring in extra information as follows. For example, we can perhaps safely exclude the time delays $\lesssim$50 years ago, since the requisite activity in Sgr A* might well have been observed on this timescale in the early radio observations of the GC (with X-ray observations in the 1980s certainly excluding delays of less than 30 years). Another good argument which reinforces this assumption is the level of 6.4-keV line emission measured in the 50 km s^{-1} and 20 km s^{-1} MCs. These clouds are most probably closer to Sgr A* than the ones studied in this paper, and should at the present time show a significant Fe-Kα line flux, if illuminated by an $L_X \sim 10^{37-38}$ erg s^{-1} within the last 30 years.

Employing the same method as for the B1 and F clouds allows us to select a rather narrow range of time delay for the B2, C and D clouds; this is the intersection of the three areas in between the vertical boundaries in the middle panel of Fig. 9. The lightcurves of the three regions match well with one another and with the results found in Sect. 4.1 for a time delay of between 70 and 82 years, for an X-ray luminosity in the range $10^{37}-10^{38}$ erg s^{-1}. The corresponding angles, and therefore distances behind the plane of Sgr A*, for these complexes are about 110°, 120° and 105° respectively, which translates into a distances of 6, 8.5 and 5 pc respectively.

We note that the B2 and D clouds may be subregions of a larger molecular complex called the *Bridge* by Ponti et al. (2010). These authors claimed to have discovered a superluminal echo in X-ray reflection, due to the propagation of the ionising front within a MC located about 60 pc behind the plane of Sgr A*. If we assume that the B2 and D clouds are part of one larger complex, then to explain the superluminal Fe-Kα line variability we need to locate the clouds behind Sgr A*, specifically at a distance greater than about 8 pc (two times the sum of the linear sizes of the regions B2 and D). There is therefore a slight disagreement between this requirement and the position inferred for clouds B2 and D using the combined results from the spectral analysis and the EW-geometry relation.

To conclude, the observed increase of the Fe-Kα line flux in the B2, D and C clouds may be well explained by a short enhancement of the X-ray luminosity of Sgr A* in the range 10^{37}–10^{38} erg s^{-1} about 80 years ago.

The A, E, DS1 and DS2 clouds: the bottom panel of Fig. 9 shows the L_X curves for the constant clouds. We can clearly see that the different segments are spread over a large area of the plot and it is not straightforward to pick out one particular pattern of activity in Sgr A* as the most likely solution. In particular, the curve for the DS2 cloud does not intersect the curves for the A and E clouds. However, the measurements do at least indicate an L_X range rather similar to that inferred from the variable clouds.

From the analysis of the geometrical constraints derived in Sect. 4.1 and plotted in Fig. 9, we can try to derive a range for the time delay (and therefore position) for the clouds; by intersecting all the different regions, we propose that the constant activity at $L_X \sim 10^{37}$ erg s^{-1} could have been experienced by Sgr A* between 130 and 100 years ago. Assuming a time delay of 120 years ago, this translates into a distance behind the plane of Sgr A* for the clouds of 12, 16, 14 and 15 pc, respectively.

Finally, in the case of the clouds with constant Fe-Kα flux, the displacement between the different curves in Fig. 9 might be explained in terms of contribution of other excitation processes to the total Fe fluorescence (see Sect. 6).

5.2. The past lightcurve of Sgr A*

The analysis of the previous section demonstrates very clearly that the Fe-Kα bright clouds within 30 pc of Sgr A* are not responding to the same outburst on Sgr A* that appears to have illuminated Sgr B2. On the contrary, the observed Fe-Kα line fluxes and inferred geometry require an X-ray luminosity of Sgr A* more typically in the range 10^{37-38} erg s^{-1} over the last 100–150 years, in very good agreement with Muno et al. (2007). Within this time frame, upwards and downwards trends lasting from a few to ten years also seem to have occurred.

As a natural step forward, we have attempt to build a long term light curve of the X-ray activity of Sgr A*, incorporating both published information and our new results – see Fig. 10. The first measurement (the green points in Fig. 10) is the X-ray luminosity required to explain the strong 6.4-keV line emission in the Sgr B2 MC. Almost since its discovery (Koyama et al. 1996), there has been a general agreement that the fluorescent of Sgr B2 requires a rather powerful X-ray flare on Sgr A*, reaching a luminosity of a few $\times 10^{39}$ erg s^{-1} a few hundred years ago. The end of this low luminosity AGN activity has recently been dated back to 100^{+55}_{-25} years ago (Terrier et al. 2010). Accordingly to Inui et al. (2009), the 6.4-keV line flux from Sgr B2 was constant for at least six years (the time of the ASCA first measurement) before the onset of the decreasing trend in 2000. In Fig. 10 we highlight the drop in the X-ray activity through green points.

Between the end of the "high state" activity and the present time, Sgr A* appears to have entered a low to intermediate state. Figure 10 shows, in a sketch form, the behaviour inferred from the measurements of the clouds within 30 pc of Sgr A*. As discussed in the previous section, this variability pattern is not unequivocally determined, although the inferred range of the X-ray luminosity is on a sounder footing. The pattern of variability depicted in Fig. 10, does allow the possibility that the regions F and B1 (together with those showing a constant Fe-Kα line emission) might be responding to the declining phase of the flare which energised Sgr B2, whereas the other XRN might be illuminated by a more recent smaller outburst.

Further evidence for the long-term downwards trend in the Sgr A* light curve is provided by the limits on the Fe-Kα flux from the 50 km s^{-1} MC. Given the proximity of this cloud to Sgr A* (∼10 pc) Ponti et al. (2010) calculate that the mean X-ray luminosity of Sgr A* in the past 60 years must have been lower than 8×10^{35} erg s^{-1}. For comparison and completeness we have also plotted in Fig. 10 the typical level of X-ray emission from the SMBH (i.e., $\sim 10^{33}$ erg s^{-1}) and the brightest flare ever detected ($L_X = 3.5 \times 10^{35}$ erg s^{-1}, Porquet et al. 2003).

In summary, in the framework of the XRN/Sgr A* scenario, we have found that the X-ray light curve of Sgr A* shows a clear decreasing trend over the last 150 years. This is not a completely smooth variation, with evidence of occasional flaring or, more precisely, for periods of relative brightening which last seeming longer than ∼5 years. Given that the light-curve is not monotonic, a much more comprehensive study of the Fe-Kα properties of the MC within the central ∼100 pc will be needed to piece together the full recent accretion history of the SMBH at the GC.

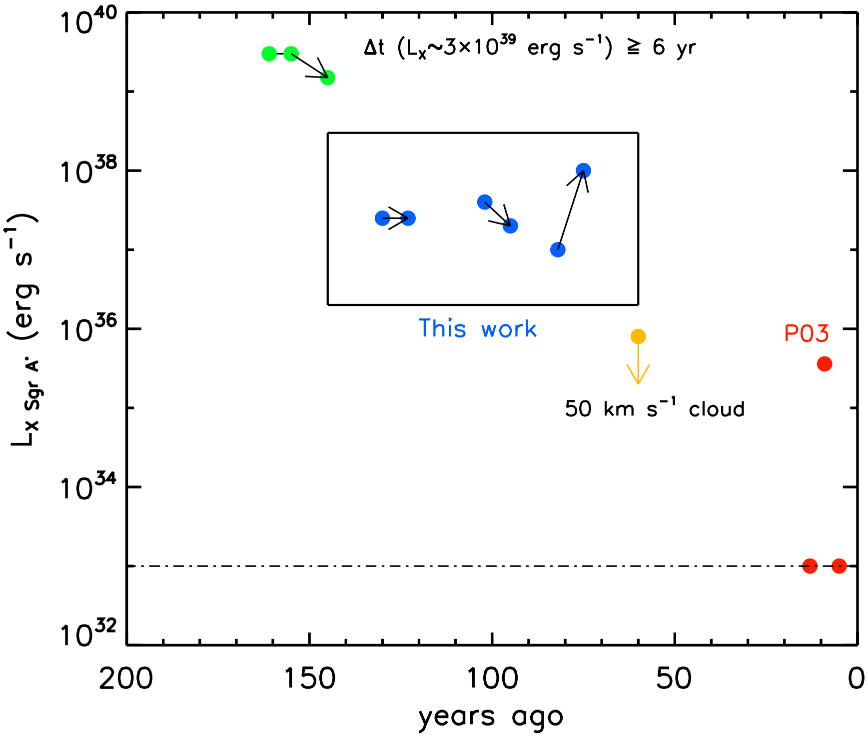

Fig. 10. X-ray light curve of Sgr A* over the past 250 years. The green points at $L_X \sim 10^{39}$ erg s^{-1} show the constraints on the Sgr A* activity inferred from the Fe-Kα measurements in the Sgr B2 cloud (see text, Inui et al. 2009; Terrier et al. 2010). The red points show the current quiescence level of Sgr A*, together with the brightest flare ever measured (Porquet et al. 2003, P03). The blue points in the box show the results of this work.

6. The CR contribution to the Fe fluorescence

6.1. Method

We have measured the 6.4-keV line flux from two extended regions to the east and west (EDE and EDW) of Sgr A*, in order to quantify the difference between the low surface brightness emission at positive and negative galactic longitudes. For this purpose we considered the two elliptical regions shown in Fig. 11, the central coordinates and sizes of which can be found in the last two rows of Table 2. In the case of the EDE region, all the sky regions coincident with the MCs previously studied have been excised, as have the 6.4-keV bright knots in the Arches cluster region (see Capelli et al. 2011b), and the Arches cluster itself (see Capelli et al. 2011a).

We have constructed MOS1&2 spectra for both the remaining EDE area and the EDW region by stacking all the data available. Here we apply a background modelling technique in fitting the four resultant spectra using the same spectral model and methodology as described in Sect. 3.2.

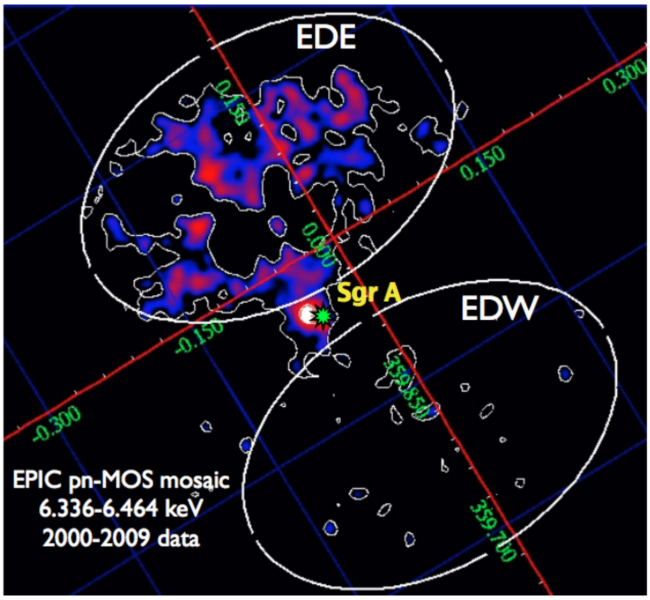

Fig. 11. A colour-coded and contoured map of the 6.4-keV line emission in GC region. The contours levels are scaled in arbitrary units. The position of Sgr A* is marked with the green star in the centre of the image, whereas the bright spot close to it is the Sgr A EAST SNR complex. The regions selected for the spectral analysis lie within the two ellipses marked as EDE and EDW. However, the bright MCs studied in this paper and in Capelli et al. (2011b), which are all located in the EDE region, have been blanked out.

6.2. Results

The results of this investigation are summarised in Table 7 and in Fig. 12 which shows the MOS2 spectra of the EDE and EDW regions and the corresponding best-fitting models. There are significant residuals near the high ionisation Si, S, Ar and Ca lines in the 2–4 keV region; these residuals may be due to a range of temperatures and/or metallicities within the extended plasma which are not well matched by the simple two-temperature model which has been applied. The Fe-Kα line flux is, however, very well determined in all these spectra. The 6.4-keV line fluxes for the EDE and EDW regions are 3.44 ± 0.06 and $1.91 \pm 0.06 \times 10^{-4}$ photons cm^{-2} s^{-1}, respectively. The average surface brightness calculated from these values are therefore $1.71 \pm 0.03 \times 10^{-6}$ and $7.8 \pm 0.3 \times 10^{-7}$ photons cm^{-2} s^{-1} arcmin^{-2}, respectively. The substantial higher level of the *underlying surface brightness* to the east of

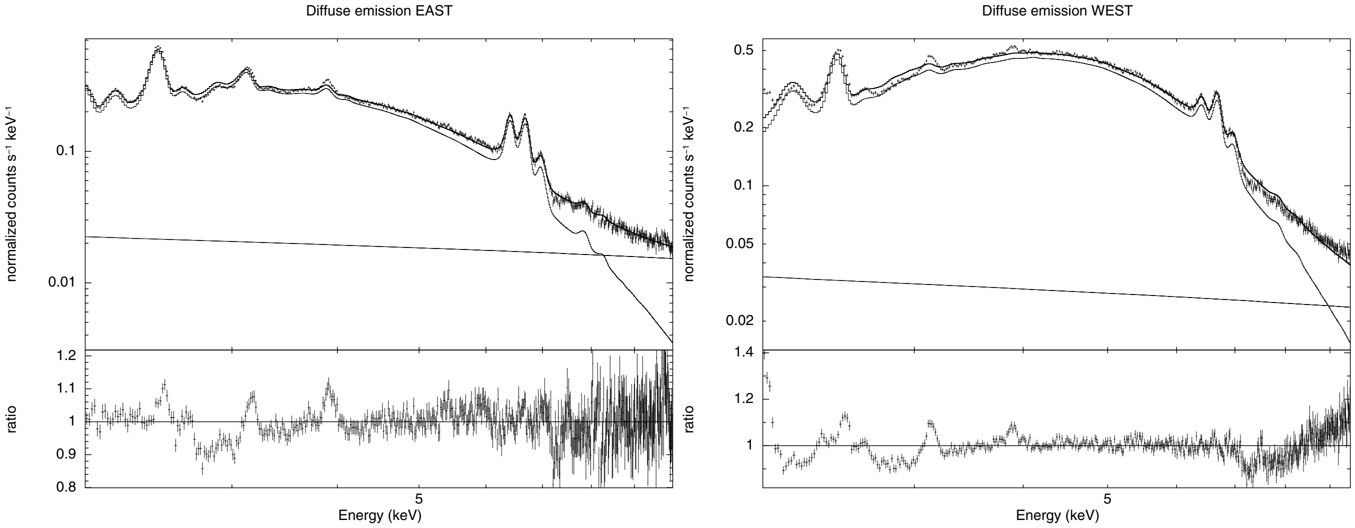

Fig. 12. *Left panel*: MOS2 spectrum of the EDE region, with the residuals in the bottom panel. The data have been collected stacking all the MOS2 spectra of the region from all the observations. *Right panel*: same for the EDW region.

Table 7. Results from the spectral analysis of the regions EDE and EDW.

	EDE	EDW
N_H	7.5 ± 0.1	9.4 ± 0.1
kT_{warm}	0.91 ± 0.01	0.356 ± 0.002
kT_{hot}	6.4 ± 0.1	6.1 ± 0.2
Γ	0.78 ± 0.04	1.0 ± 0.1
norm	$5.5 \pm 0.1 \times 10^{-3}$	$1.61 \pm 0.01 \times 10^{-2}$
F_{64}	$3.44 \pm 0.06 \times 10^{-4}$	$1.91 \pm 0.06 \times 10^{-4}$
EW	0.37 ± 0.02	0.077 ± 0.002

Notes. The quoted parameter values are the weighted means of those obtained from individual MOS1 and MOS2 spectra. The units of N_H are 10^{22} cm^{-2}, the temperatures of the two plasmas are quoted in keV, the normalization of the non-thermal component has units of photons cm^{-2} s^{-1} keV^{-1} at 1 keV and the Fe-Kα line flux has units of photons cm^{-2} s^{-1}.

Sgr A*, compared to the situation to the west, is also apparent in Fig. 11.

The fact that the underlying diffuse Fe-Kα emission at positive Galactic longitudes is roughly a factor two more intense than that measured at the corresponding negative longitudes is an interesting result. In particular it can be directly compared with the very-high energy γ-ray map of the GC region obtained with the HESS telescope (Aharonian et al. 2006). The TeV emission shows a strong enhancement to the East of Sgr A*, with a peak close to the centre of our EDE region (see also Yusef-Zadeh et al. 2007b).

The TeV emission most likely arises from the hadronic interactions of CR with the molecular material in the CMZ, which prompts the question as to whether the underlying level of the 6.4-keV emission to the east of the GC might similarly be the result of CR bombardment of the MCs (albeit by CR particles of very different energy to those giving rise to the TeV signal). A further step is then to conjecture that the non-varying emission pedestals seen in some of the 6.4-keV bright MCs might also be the result of the same CR bombardment process. Consider, in this context, the B2 and D regions (see Fig. 2), which apparently compose the region referred to by Ponti et al. (2010) as the *Bridge*. The first three data points (covering the period 2002–2004) in their 6.4-keV light curves (see Table 3 and Fig. 4) are consistent with constant levels of 1.1 ± 0.1 and $0.8 \pm 0.1 \times 10^{-5}$ photons cm^{-2} s^{-1} respectively. These measurements translate to surface brightnesses of 5.2 ± 0.5 and $4.5 \pm 0.6 \times 10^{-6}$ photons cm^{-2} s^{-1} arcmin^{-2}, which are compatible with each other, but higher than the mean 6.4-keV diffuse surface brightness calculated for regions EDE and EDW. If one then compares the 6.4-keV surface brightness of the B2 and D pedestals, the EDE region (after excluding bright MCs) and the EDW region, the ratio 6.4/2.2/1.0 is obtained. In a similar way, if we look at the contours of the TeV emission map (Fig. 12a in Yusef-Zadeh et al. 2007b), we can see that there is a remarkable agreement with this 6.4-keV surface brightness scaling. The brightest TeV emission is detected in a region roughly matching the physical extent of the B2 and D clouds (innermost contour of Fig.12a in Yusef-Zadeh et al. 2007b), whereas the EDE region is well delimited by the third contour of the TeV surface brightness distribution, and the EDW region by the next two (lower) contour levels.

We interpret the above as an indication that CR bombardment may well play a role in exciting X-ray fluorescence in the GC region. Specifically this process could potentially give rise to the baseline levels (i.e., emission pedestals) noted in several of clouds with variable 6.4-keV emission. In addition, for clouds lying outside of the regions where the X-ray illumination is most intense, CR bombardment might be the dominant source of fluorescence excitation (see also Capelli et al. 2011b). Plausibly this might include some of the more diffuse structures apparent in the Fe-Kα maps.

Unfortunately, it is difficult to disentangle from X-ray studies alone, what contribution CR bombardment makes to the total 6.4-keV line emission. Nevertheless, we can investigate this issue by assuming (i) that CR electrons with energies in the range 10 keV^{-1} GeV are the cause of the underlying X-ray fluorescence seen in the GC and that (ii) the concentration of these particles is relatively uniform across the region of the CMZ studied in this paper. Table 8 summarises the physical parameters of all the GC clouds and structures which are known to be Fe-Kα emitters plus some upper limits for several other prominent clouds. For the variable clouds, we have

Table 8. Physical parameters for the MCs and other regions in the CMZ region which display Fe-Kα emission.

Cloud	N_{HC}	F_{64}	Area
A	$18.4^{+1.4}_{-2.6}$	2.5 ± 0.1	2.2
B1	$10.2^{+2.3}_{-2.0}$	2.3 ± 0.3	2.6
B2	$12.3^{+3.0}_{-2.7}$	2.1 ± 0.1	1.9
C	$5.8^{+2.3}_{-1.9}$	1.2 ± 0.2	2.0
D	$13.2^{+5.0}_{-4.8}$	1.2 ± 0.2	1.8
E	$9.6^{+1.7}_{-1.3}$	2.0 ± 0.1	2.9
F	$9.2^{+2.7}_{-2.3}$	13.0 ± 1.0	14.6
DS1	$15.5^{+3.9}_{-3.3}$	1.5 ± 0.1	3.7
DS2	14.5 ± 2.3	$2.6^{+0.2}_{-0.1}$	6.5
EDE	1.5	34.0 ± 1.0	202.9
EDW	3.4	19.0 ± 1.0	243.9
N	4.0	0.39 ± 0.04	0.5
S	2.0	0.69 ± 0.05	0.5
SN	2.0	0.46 ± 0.04	1.0
$\mathrm{DX_{CR}}$	2.0	0.16 ± 0.05	0.8
$\mathrm{DX_{X}}$	2.0	0.47 ± 0.09	0.8
Sgr B2†	58.0 ± 3.0	10.0 ± 1.0	4.5
50 km s$^{-1\ddagger}$	9.0	≤ 1.7	9.2
G0.162§	2.0	0.2 ± 0.1	3.1
G0.174§	2.0	0.7 ± 0.1	4.5
G359.43††	10.0	0.6 ± 0.1	7.1
G359.47††	10.0	0.9 ± 0.1	6.9

Notes. The table lists the cloud column density (in units of 10^{22} cm^{-2}), the Fe-Kα line flux (in units of 10^{-5} ph cm^{-2} s^{-1}), and the sky area subtended by the MC or feature (in arcmin^2). $^{(\dagger)}$ Terrier et al. (2010). $^{(\ddagger)}$ Ponti et al. (2010). $^{(\S)}$ Fukuoka et al. (2009). $^{(\dagger\dagger)}$ Nakajima et al. (2009). The top section of the table is devoted to the MCs studied in this work, whereas the regions in the second panel are those in the vicinity of the Arches cluster considered by Capelli et al. (2011b). Parameters for the clouds in the lower section are taken from the literature (see the notes below). In the case of the MCs with a variable Fe-Kα line flux, we list the minimum value on record. Error ranges for the N_{HC} values are not available in all the cases, specifically when the values are estimates or assumed values.

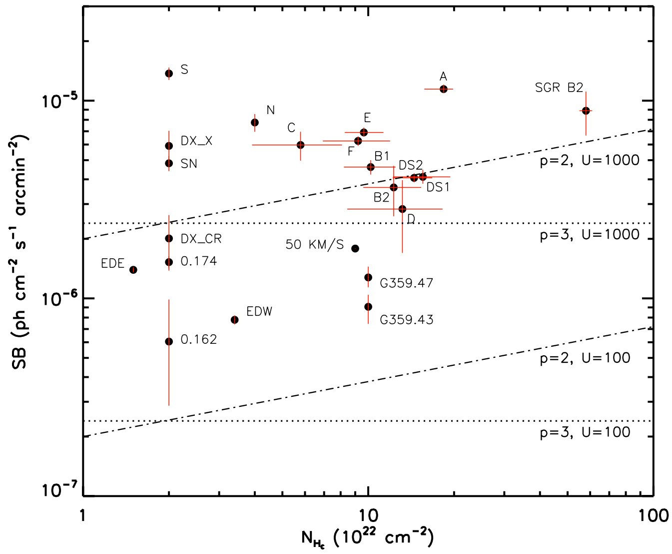

Fig. 13. Surface brightness of the Fe-Kα line measured from the MCs in the CMZ, plotted against their estimated column density, N_{HC}. The labels indicate the identity of each cloud, while the lines represent model predictions for CR electron densities of 100 and 1000 eV/cm^3 (lower and upper lines respectively), for assumed slopes of the electron energy spectrum of $p = 2$ (dotted lines) or $p = 3$ (dashed lines). *CR contribution band* as described in the text.

considered the minimum 6.4-keV line flux recorded to date; for the Sgr B2 cloud we considered the Fe-Kα flux value as extrapolated for the year 2010 from Fig. 4 in Terrier et al. (2010).

In Fig. 13, we have plot the Fe-Kα surface brightness of each cloud (in photons cm^{-2} s^{-1} arcmin^{-2}) versus the estimated column density. The contribution of CR electrons to the observed Fe-Kα surface brightness of various GC clouds has been discussed by Yusef-Zadeh et al. (2007a). Using the same methodology as (Yusef-Zadeh et al. 2007a, in particular their Fig. 13 and Eq. (10)), we obtain the estimates for the CR contribution shown in Fig. 13 as straight lines; here, U and p represent the energy density of the LECRe population and the photon index of the power law energy distribution of the injected electrons (E^{-p}), respectively. Figure 13 has three main regions. The clouds with column densities higher than $\sim 5 \times 10^{22}$ cm^{-2} and Fe-line intensities brighter than $\sim 5 \times 10^{-6}$ photons cm^{-2} s^{-1} arcmin^{-2}, such as Sgr B2 and the bright nebulae studied in the present work, are very likely excited by X-ray illumination, i.e., are bona fide XRN. At similar brightness levels, but somewhat lower N_{HC}, lie the MCs in the vicinity of the Arches cluster; as we have shown in our previous study (Capelli et al. 2011b), the Fe fluorescence within these clouds is most likely energised by particles emanating from the Arches cluster itself (CR electrons or protons). The third region, lying between the predictions for CR electron energy densities of 100–1000 eV/cm^3, could also plausibly corresponded to clouds primarily excited by CR bombardment.

A remarkable result shown by the plot in Fig. 13 is that, when considering the constant (minimum) base level of the variable Fe-Kα line emission in regions B2 and D, this falls into the CR contribution region delimited by the straight lines in Fig. 13; this strongly suggest that a CR component might be present in all lightcurves studied in this work, and it is of a strategic importance to carry out studies on the CR population in the innermost CMZ in order to definitely disentangle the contribution due to the two sources (CR and Sgr A*), in primis for better constraining the past activity of the SMBH.

Due to the high uncertainties in the parameters plotted in this figure, we do not want to rely too much on it in deriving all properties of the MCs we considered, nor putting a net separation between the two excitation processes (which could be present in tandem in some of the clouds). However, we think that some conclusions about the CR contribution to the Fe fluorescence observed in GC MCs can be drawn already at this stage (see Fig. 13):

- We can safely conclude that the 6.4-keV line emission measured in the A to F complexes is far too high to be only due to CR bombardment. Detections of the line variability and the absorption feature at the Fe-K edge give further confirmation of the XRN nature of these MCs, although a component to the Fe fluorescent seems to be present.
- The EDE and EDW diffuse regions are most likely to be illuminated by LECRs, where the surface brightness gap may reflect the averaged dishomogeneity in the CR distribution.
- The Sgr C MC is very different from Sgr B2 and the XRN in the immediate vicinity of Sgr A*; the Fe-Kα surface brighteness is about a factor 20 lower than what measured in Sgr B2, and a factor of 10 lower than what measured in the A-F clouds. Assuming the same illumination scenario as for the Sgr B2 cloud, we calculate that the total distance of the

Sgr C clumps G359-43 and G359.47 should be as high as 500 to 700 pc, which seems very unlikely. Moreover, all the X-ray observations performed on Sgr C measured the same SB of the 6.4-keV line over about 10 years; we therefore propose that the description of the Fe fluorescence in the Sgr C cloud as due to LECRs bombardment as a likely possibility.
- The complexes G0.162 and G0.174 well lie within the *CR band*; as already proposed by Fukuoka et al. (2009), the 6.4-keV line in the former is likely to be due to CR bombardment, given the relative vicinity to the radio arc. On the other hand, these autors argued that G0.174 is an XRN, whose origin is still not confirmed. For what concerns the plot in Fig. 13 we can see that while G0.162 is well within the *CR band*, G0.174's surface brightness is significantly higher and other studies should be performed in order to prove the XRN nature of this MC. An Fe-Kα EW of 0.9 ± 0.2 keV is not enough to disprove either hypothesis on the Fe fluorescence mechanism.

Of course, the starting premise of a constant CR concentration is far from being correct, but a plot as the one shown in Fig. 13, if nothing else, has the merit of illustrating the order of magnitude spread in surface brightness across all the GC clouds bright in the 6.4-keV line.

7. Discussion

7.1. X-ray reflection nebulae

The XRN concept was first suggested by Sunyaev et al. (1993) and later developed by Koyama et al. (1996), Sunyaev & Churazov (1998) and Murakami et al. (2000). In this scenario, a powerful transient X-ray source supplies the primary photons needed to produce the fluorescence observed from the GC molecular clouds. The whole phenomenology, both the line flux and the topology of the Fe-Kα line emission, of the Sgr B2 giant molecular cloud is well explained in this scenario. In this context Sgr A* must have been bright roughly 150 years ago (based on the projected separation of Sgr B2 and Sgr A*) reaching an X-ray luminosity of $2–5 \times 10^{39}$ erg s^{-1} (Terrier et al. 2010). This is about 10^5 times lower than the Eddington luminosity for a SMBH with the mass of Sgr A*, and so is entirely plausible.

If Sgr A* is indeed the primary source of the ionising photons for Sgr B2 then, by implication, the Fe-Kα emission observed in the more immediate vicinity of Sgr A* might similarly serve as a tracer of past outbursts in this source. Ponti et al. (2010) have reported the complex nature of the variability seen in the 6.4-keV bright filaments with 30 pc of Sgr A* and have suggested a scenario in which these clouds are illuminated by the same outburst responsible for the Sgr B2 Fe fluorescence.

This picture has to date been the favoured explanation of the 6.4-keV line variability seen in the GC MCs. In broad terms our study of the MCs in the immediate vicinity of Sgr A* serves also as a confirmation of many of the observational details reported by Ponti et al. (2010). However, our conclusion is quite different, namely that the luminosity required to ionise the MCs studied in this paper must be at least one order of magnitude lower than the outburst which is currently illuminating Sgr B2. Most importantly, the derived X-ray lightcurve of Sgr A* over the last ~150 years appears to exhibit occasional episodes of brightening, which last at least 5 years, superimposed on a general decreasing trend.

The main breakthrough that sets our paper apart from earlier contributions on this topic is the direct measurement of the column density and the Fe abundance of the MCs in our sample, which are the two fundamental parameters for the study of the XRN behaviour. Using this approach we were able to study the 3D distribution of the MCs in the innermost CMZ in two independent ways, which returned consistent results and therefore reinforced our findings.

First, in Sect. 4.1 we used our measurements of the EW of the 6.4-keV line in order to calculate, within a theoretical framework, the average Fe abundance within the selected MCs. Our results show that the metallicity of the MCs in our study is supersolar with $Z_{\rm Fe} = 1.6 \pm 0.1\ Z_{\odot}$, a value which is in very good agreement with previous estimates (e.g. Nobukawa et al. 2010, 2011). Secondly, in Sect. 4.2 we determine the column densities of the MCs in our sample directly from the fitting of their X-ray spectra. Our X-ray derived $N_{\rm H_C}$ values are consistently higher than those estimated from CO-CS measurements. Of course, measurements based on molecular lines require the assumption of a thermal temperature for the molecular gas which is not known a priori, and do not take into account abundance variations in molecules such as CS. Another possible way to estimate the $N_{\rm H_C}$ of a molecular cloud is the comparison with mm continuum maps of dust emission; however, here one meets severe difficulties in picking out relatively small clouds against the general continuum brightness of the GC region. Also the gas-to-dust ratio in the GC environment may differ from that found in other regions of the Galaxy.

Both the high value of the EW of the 6.4 keV Fe-Kα line and the strong suppression of the non-thermal X-ray continuum at the Fe-K edge (at 7.1 keV) supports the view that the brightest clouds in our sample are true XRN. Our determination of the spectral slope of the ionising continuum to be $\Gamma \approx 1.9$ also matches the likely spectral form of the continuum X-ray emission emanating from Sgr A*, which illuminates the Sgr B2 cloud (e.g. Revnivtsev et al. 2004).

In the context of the activity of Sgr A* in the recent past, we have two important new results:

- In a pure reflection scenario where Sgr A* supplies the primary photons at a constant luminosity, one might expect the 6.4-keV surface brightness of the densest clouds in the inner 30 pc region to be between 20–50 times higher that of Sgr B2, commensurate with the inverse square fall-off in the illuminating intensity. In fact there is no evidence for such an effect; on the contrary none of the central region clouds have 6.4-keV surface brightness values in excess of that on Sgr B2 (see Fig. 9). More quantitatively, we show that the Fe fluorescence of the MCs in our sample can be explained in terms of the X-ray luminosity $L_{\rm X}$ of Sgr A* reaching levels of between 10^{37} and 10^{38} erg s^{-1} over the last 150 years. This is more than an order of magnitude lower than that required to explain the observed fluorescence of the Sgr B2 cloud.
- Within the last 150 years the X-ray activity of the primary source can be characterised as a declining trend upon which occasional episodes of brightening, lasting at least 5-years, are superimposed. A scenario in which the observed pattern of activity might arise is suggested by the very recent discovery of a dust cloud on its way towards its likely final accretion onto Sgr A* (Gillessen et al. 2012). Unfortunately, there is no detailed knowledge of the physical parameters of this cloud, and the X-ray luminosity which might ensue following this accretion event is hard to predict with any certainty. Nevertheless, on timescales of 10's to 100's of years, accretion events triggered by the capture of passing clouds would seem to be a very likely occurrence, particularly since

the amount of interstellar gas in the accretion flow onto the SMBH at the GC is sufficient, in principle, to produce $L_{\rm X} \sim 10^{40}$ erg s^{-1} (Cuadra et al. 2005).

7.1.1. Association of the X-ray transient XMMU J174554.4-285456 with region C

The X-ray transient source XMMU J174554.4-285456 was first detected with *XMM-Newton* during an outburst on 2002 October 3rd (Porquet et al. 2005). Repeated observations of the GC region performed with *Chandra* later revealed this source to be bright in June-July 2004 (Muno et al. 2005; Wang et al. 2006). A closer inspection to the *XMM-Newton* dataset employed in this work revealed the presence of this source in the March 2004 data. So far, the nature of this peculiar X-ray binary has not yet been ascertained. The ratio between the X-ray luminosity at the outburst and in the quiescence state is about 10^4. For this reason, we decided to investigate whether the measured fluxes of the 6.4-keV line from the region C could be due (in part) to the flaring activity of this X-ray binary.

The observed 6.4-keV line flux lightcurve from the region C shows a step behaviour (see Fig. 4). Dividing the six epochs into two, we obtain weighted means of 0.8 ± 0.1 and $1.2 \pm 0.1 \times 10^{-5}$ photons cm^{-2} s^{-1}, respectively. A closer inspection to the full band X-ray image from observations 0202670501 and 0202670601 shows the presence of the X-ray transient source XMMU J174554.4-285456 within the bounds of region C (see Fig. 14, Porquet et al. 2005). The best spectral model has been found to be an absorbed powerlaw, with a $\Gamma = 1.7 \pm 0.2$ and a very high column density ($N_{\rm H_C}$) of $14.1^{+1.0}_{-1.4} \times 10^{22}$ cm^{-2}. The flaring X-ray luminosity of this source was 1.5×10^{35} erg s^{-1} in the 0.5–10 keV band (Porquet et al. 2005).

Assuming the enhancement in the Fe-Kα light curve is due to the brightening of XMMU J174554.4-285456, we calculate the requisite distance of the binary to be of the order of 2 pc. Given the high $N_{\rm H_C}$ value measured towards this source, we favour the geometry in which the MC lies in the line of sight between us and XMMU J174554.4-285456. In this setting, the measured time delay between the first reported flare on the binary (October 2002) and the onset of enhanced 6.4-keV flux (4.5 years), the size of the cloud (3.7 pc) and the distance of the X-ray source (2 pc) represent a consistent picture.

In summary the Fe fluorescence of region C may, in principle, be explained without recourse to the XRN/Sgr A* paradigm. Its base (or pedestal) level of Fe-Kα emission might arise from CR particle bombardment (see Sect. 6) upon which is superimposed a component due to X-ray irradiation of the cloud by a (very) nearby transient source XMMU J174554.4-285456. Potentially this is the second XRN positively associated with an X-ray transient source in the GC region (Capelli et al. 2011b).

7.2. CR particle bombardment

This model has been proposed and discussed by Valinia et al. (2000), Predehl et al. (2003), Yusef-Zadeh et al. (2007a) and Dogiel et al. (2009). In this context, the primary source of the Fe fluorescence are CR particles, potentially with a variety of compositions, origins and energies. While the photoionisation cross-section is a steep function of the energy of the primary photon, the cross-section for collisional ionisation is a relatively smooth function of the energy of the incident particle. For electrons with energies in the range 10−100 keV and protons with energy between 10 and 100 MeV, the cross section for collisional ionisation of Fe remains relative close to its maximum value, i.e. these are the energy ranges over which the particle bombardment most likely occurs. However, the number of particles will fall sharply with energy so one might not expect the major contribution to be due to the highest energy component.

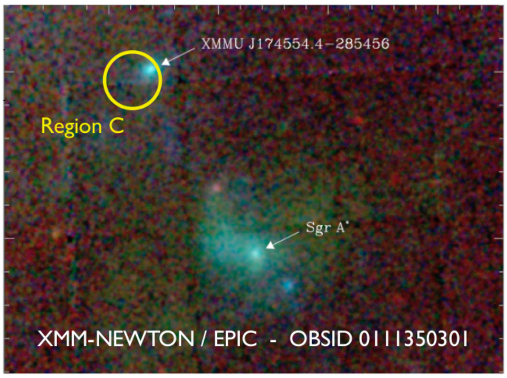

Fig. 14. *XMM-Newton*/EPIC colour image of the X-ray transient XMMU J174554.4-285456 (Porquet et al. 2005). The colour coding is as follows: red (0.2–2 keV), green (2–5 keV) and blue (5–10 keV). The yellow circle on the top of the image shows region C.

Although electrons have been historically favoured as the source of ionisation of MCs in the CMZ, electrons with a kinetic energy of some tens of keV can barely penetrate the target clouds since they are stopped by a column density of only $\sim 10^{21}$ cm^{-2}. As a consequence, fluorescent emission via electron bombardment most likely takes place within the surface layers of a dense cloud. On the other hand, protons have a much larger penetrating power than electrons; a 30 MeV proton is stopped by a column density higher than 10^{22} cm^{-2}, a value approaching the column densities found in the GC region. Accordingly, protons may be as, or more, important than electrons as a source of ionisation of MCs, although peculiar locations (the Radio Arc, the Arches cluster) might reveal different mechanisms at work.

Very recently, Capelli et al. (2011b) showed that in the Arches cluster region there are MCs similar to those studied in this paper in terms of their Fe-Kα surface brightness, size and inferred density. In fact, it is very likely that the bulk of the underlying fluorescence in these clouds is induced by particle bombardment, with an estimated CR energy density of about 50–100 eV/cm^3, that is two orders of magnitude higher than that estimated for the Galactic plane in general (see Capelli et al. 2011b); the Arches cluster is, of course, the most likely site of the requisite particle acceleration.

Our results confirm that a major contribution to the Fe-Kα line emission in the MCs in our sample comes from X-ray photoionisation. However, we argue that a significant contribution from CR bombardment might be present in the spectra of these XRN – as discussed in Sect. 6.

To support this hypothesis, we presented in Fig. 13 possible evidence for the underlying particle ionisation component. In a plot of the Fe-Kα surface brightnesses against the cloud column density of the MCs, we were able to distinguish different regions of parameter space in which X-ray illumination and CR particle bombardment might operate as the primary source of the Fe fluorescence. However, much more information is required in relation to the CR energy density and spatial distribution in the innermost CMZ is required if we are to understand the relative importance of the various excitation processses.

The Fe-Kα line emission from particle bombardment is generally expected to show a constant lightcurve. However, it is at least conceivable that time variable magnetic fields in the filaments and threads and/or time variable CR fluxes might induce measureable changes over timescales upwards of a few years in some compact molecular structures. Evidence for such behaviour could come from variability studies of the radio continuum in narrow radio emitting filaments confined by magnetic pressure, although of course in such cases the particles will be electrons with relativistic energies emitting synchrotron radiation.

Oka et al. (2010) discovered high velocity compact clouds in the GC region which show a CO $J = 3$–$2/J = 1$–0 intensity ratio higher than that typically found in the Galactic disc. These features are likely to be knots of shocked molecular gas, heated by energetic events such as supernovae explosions. The distribution of these clumpy structures correlates well with the location of the molecular filaments we have studied in this work. The same is true for the Sgr C molecular cloud (Oka et al. 2010). This correlation suggests a close relation between these shocked molecular complexes and the Fe-Kα line emission, since shocks internal to the clouds act as particles accelerators. Moreover, Muno et al. (2008) showed that there are many physical processes active in the GC region which appear to produce diffuse X-ray features. For example, these authors discovered ≈20 candidate pulsar wind nebulae within 20 pc of Sgr A*, which are among the best established sites of CR acceleration. The particle bombardment hypothesis places few direct constraints on the cloud/particle flow geometry, given that particle will travel along the local field lines. Nevertheless this scenario does provide at least a plausible explanation of why the brightest Fe fluorescence regions are sometimes located on the farside of the cloud as viewed from Sgr A* (for example, in Sgr C, Yusef-Zadeh et al. 2007a).

8. Conclusions

We have studied the X-ray properties of selected molecular clouds and filaments to the east of Sgr A* at a projected distance of ≈8–30 pc.

- *Fe-Kα topology*: we have demonstrated that the Fe-Kα emission delineates both compact and more diffuse structures. We have studied the temporal and spectral properties of 9 clouds; three of which are newly studied (regions C, DS1 and DS2).
- *Fe-Kα variability*: significant variability is seen from some of the molecular clouds, although the pattern is by no means a simple one. Our Fe-Kα flux and variability measurements agree reasonably well with previous published results, although in the case of one cloud (B1) we measured a decrease of the Fe-Kα line flux, in contrast with what found previously.
- *Fe-Kα surface brightness*: we measure the surface brightness of the 6.4-keV line to be of the same order of magnitude in all the molecular filaments we have studied. Typically the observed variability only involves a factor of two change. In the Sgr A*/XRN scenario, the surface brightness of the filaments might be expected to decline with distance from Sgr A*. This issue is resolved by our finding that the X-ray luminosity of Sgr A* has declined substantial over the last 150 years.
- *Fe-Kα EW and Fe-K edge measurements*: we measured a high value of the EW of the 6.4-keV line from all the MCs in our sample, consistent with an origin of the bulk of the fluorescence in photoionisation. Moreover, all the clouds show an absorption feature at the Fe-K edge energy of 7.1 keV.
- *Spectral hardness of the reflected continuum*: the spectral shape of the reflected/ionising X-ray continuum emission associated with the Fe fluorescence is found to be $\Gamma \approx 1.9$, a result compatible with the XRN/Sgr A* scenario, since this is a value rather typical of that found in AGN.
- *Fe abundance*: we use the measured EW values of the Fe-Kα line in our sample of MCs to calculate the average Fe abundance (relative to solar). We show that $Z_{\rm Fe} = 1.6$, a result which is consistent with the general finding that a higher than solar metallicity characterises all the ISM phases in the GC region.
- *Column density through the MCs*: we have employed a relatively direct method to calculate the hydrogen column density, $N_{\rm H_c}$, within the MCs. This is based on the joint modelling of the low-energy absorption and the absorption at the Fe-K edge imprinted on the incident continuum in its passage through the cloud (both up to and after the point of scattering). This approach benefits from prior knowledge of the relatively iron abundance, $Z_{\rm Fe}$, in the cloud. The column densities so calculated are close to 10^{23} cm^{-2} and, in most cases, significantly higher than those inferred in previous studies, which made use of radio molecular line measurements.
- *The past X-ray activity of Sgr A**: based on our study of the 6.4-keV line emission properties of the MCs in the inner 30 pc of the GC region, we outline a model for the X-ray emission of Sgr A* encompassing the last ~150 years. Over this period the X-ray luminosity has declined from an apparent peak of ~10^{39} erg s^{-1} roughly 150 years ago, to 10^{37-38} erg s^{-1} perhaps 100 years ago, down to typically 10^{33-35} erg s^{-1} at the present time. This decreasing long-term trend has, however, been punctuated by counter-trend episodes of brightening by factors of a few over timescales in excess of ~5 years.
- *Cloud C – an XRN energised by a transient source?*: we have found that the 6.4-keV line flux variability measured from cloud C could also be associated with the transient X-ray source XMMU J174554.4-285456. In this scenario, the Fe fluorescence in this complex is composed of a steady non-zero level, possibly produced by the interaction of CR with the ambient gas plus a superimposed contribution due to the localised variable X-ray irradiation. If this picture is confirmed, this is the second XRN found in the GC region which has been illuminated by a transient X-ray source (Capelli et al. 2011b).
- *Low surface brightness 6.4-keV line emission*: we have found a good correlation between the TeV emission and the Fe-Kα line emission observed on arcminute scales in the inner CMZ. Specifically we measured diffuse, low surface brightness emission to the east of Sgr A*, which seems to permeate the whole region between the Sgr A* and the giant Radio Arc. A pedestal (i.e. constant) fluorescence component might in fact be present in all the lightcurves which show a varying Fe-Kα line flux. We have also shown that this diffuse low surface brightness 6.4-keV line emission correlates quite well with the contours of the brightest features seen in TeV γ-rays. This suggests that CRs may contribute to the ionisation and fluorescence of cold gas in this region.
- *CR contribution*: we presented arguments in favour of a CR contribution to the total Fe fluorescence in the GC MCs. In particular, LECR may be responsible for the constant of 6.4-keV line emission observed in several structures (including the Bridge), as well as in other regions of the CMZ, like the Arches cluster, the Radio Arc and Sgr C. We suggest that further study of the Fe-Kα surface brightness versus

$N_{\mathrm{H_C}}$ relation for GC clouds will help reveal the contribution of CR to the Fe-K fluorescence observed in the GC region.

We are far from unveiling the full mystery of the Fe fluorescence observed in the GC region. It will be of great importance in the future to continue to monitor the Fe-Kα line emission from the MCs in the CMZ so as to better characterise the past activity of Sgr A*. Future X-ray observations can also complement studies in different energy domains, from the radio band (continuum and lines) up to the TeV regime, which aim to fully chart the influence of CR particles on the GC environment.

Acknowledgements. This work is based on observations performed with the *XMM-Newton* satellite, an ESA mission with contributions funded by ESA Member Countries and NASA. We thank the referee for useful comments and suggestions. R.C. would like to thank all people involved in this work.

Appendix A: Dealing with the EPIC detector background

Within an *XMM-Newton*/EPIC dataset, two main background components can be defined, namely particle-induced events and photon-induced events. Solar-flare particles and CRs are responsible for the continuum element of the non X-ray Background (NXB), as well as for the strong instrumental lines (Leccardi & Molendi 2008). A further minor component within the particle-induced background is due to quiescent soft protons (QSP). These are particles which enter the optics and are focused onto the detector; they are mostly filtered during the GTI selection, but is likely that there is a low-level residual component in the screened event file. In the case of the photon background from the sky, the main components are the hard X-ray emission along the plane of the Galaxy (the Galactic ridge emission both in the foreground and extending beyond the GC), and also the extragalactic cosmic X-ray background (CXB). We did not take into account the Galactic halo since its emission is negligible above 2.0 keV (Leccardi & Molendi 2008). The difficulty of carrying out a systematic analysis with a careful characterisation of the background is that the particle-induced background, which is the dominant component in the hard X-ray band, changes both spatially on the detector and in time throughout the duration of the mission. Given the focus of our investigation, there was a clear requirement that all the datasets should be analysed in a very systematic fashion. This led us to consider the advantages and disadvantages of the standard methods of dealing with the background in *XMM-Newton* observations.

Local background subtraction: this procedure consists of selecting a region in the same image/dataset close to the source of interest; it is certainly the best choice for the analysis of a bright point source. The fact that we are dealing with extended sources, which are close to each other, forces us to select a region well separated from the position of the filaments under study. This may, potentially, produce a large discrepancy between the intensity of the instrumental lines in the source and in the background spectra, especially in the PN camera (e.g. at the Cu line at 8.05 keV), generating strong systematic errors which are difficult to deal with. As a further difficulty, the presence of the Galactic ridge emission throughout the whole FOV prevents us from selecting a region for the background with a low surface brightness.

Blank sky fields: Blank sky files are constructed using a superposition of pointed observations of regions of the sky without contamination by bright sources (Carter & Read 2007). They contain most of the background components listed above, like the particle induced NXB and the CXB. To study an extended source, we tried to cast the blank event file onto the sky at the position of our observations using the *skycast* script. In doing so, we are able to select the same detector region for the production of both the source and the background spectra. This method has the great advantage of completely avoiding the possibility of having different instrumental lines intensities, but the various components of the background can all vary in different ways over long time periods. So far, the blank sky files available are for observations done before revolution ≈1200, that is early 2007 (A. Read, priv. comm.). We tested the public blank fields in our spectral analysis. While for revolutions earlier than 1200 the instrumental background subtraction was feasible, the spectra obtained with later data still show strong contamination, which is easily noticeable in the intense Cu Kα line at 8.05 keV in the PN camera. Since we are using *XMM-Newton* observations taken over a period of ≈10 years, the blank sky event files technique cannot be used for our purposes.

Background modelling: this technique requires a careful characterisation of all the background components. The strong advantage of modelling the background rather than subtracting it, is that many of the systematics may thereby be avoided. De Luca & Molendi (2004) and Leccardi & Molendi (2008) studied in detail the properties of the particle-induced background for the MOS cameras, giving a spectral shape to both the continuum and the line emission. Modelling the background, instrumental and cosmic components we can, in principle, account for all the photons collected by the instrumentation and make every photon count.

On the basis of the above, we decided to follow the background modelling technique for measuring the temporal variability of the Fe-Kα emission. With this choice we did not consider further the EPIC-PN data, but worked only with MOS cameras. Up to the present, a self-consistent and exhaustive characterization of the background for EPIC-PN camera has not been developed, mainly because the fraction of out-of-time events in the PN CCDs is not negligible and the Out FOV region is much smaller compared to the one in the MOS detectors. Moreover, MOS cameras are better suited to the study of extended sources because of the lower level of the instrumental background (which is most likely a consequence of the different CCD structure). However, for the analysis of the stacked spectra the excellent hard response of the PN camera outweighed these considerations and for this study we employed the PN spectra and local background subtraction.

References

Abbey, T., Carpenter, J., Read, A., et al. 2006, in The X-ray Universe 2005, ed. A. Wilson, ESA Spec. Publ., 604, 943
Aharonian, F., Akhperjanian, A. G., Bazer-Bachi, A. R., et al. 2006, Nature, 439, 695
Amo-Baladrón, M. A., Martín-Pintado, J., Morris, M. R., Muno, M. P., & Rodríguez-Fernández, N. J. 2009, ApJ, 694, 943
Capelli, R., Warwick, R. S., Cappelluti, N., et al. 2011a, A&A, 525, L2
Capelli, R., Warwick, R. S., Porquet, D., Gillessen, S., & Predehl, P. 2011b, A&A, 530, A38
Carter, J. A., & Read, A. M. 2007, A&A, 464, 1155
Cash, W. 1979, ApJ, 228, 939
Cuadra, J., Nayakshin, S., Springel, V., & Di Matteo, T. 2005, MNRAS, 360, L55
De Luca, A., & Molendi, S. 2004, A&A, 419, 837
Dogiel, V., Cheng, K., Chernyshov, D., et al. 2009, PASJ, 61, 901
Fukuoka, R., Koyama, K., Ryu, S. G., & Tsuru, T. G. 2009, PASJ, 61, 593
Ghez, A. M., Salim, S., Weinberg, N. N., et al. 2008, ApJ, 689, 1044
Gillessen, S., Eisenhauer, F., Trippe, S., et al. 2009, ApJ, 692, 1075
Gillessen, S., Genzel, R., Fritz, T. K., et al. 2012, Nature, 481, 51

Handa, T., Sakano, M., Naito, S., Hiramatsu, M., & Tsuboi, M. 2006, ApJ, 636, 261

Inui, T., Koyama, K., Matsumoto, H., & Tsuru, T. G. 2009, PASJ, 61, 241

Koyama, K., Maeda, Y., Sonobe, T., et al. 1996, PASJ, 48, 249

Koyama, K., Hyodo, Y., & Inui, T. 2006, J. Phys. Conf. Ser., 54, 95

Koyama, K., Hyodo, Y., Inui, T., et al. 2007, PASJ, 59, 245

Koyama, K., Inui, T., Matsumoto, H., & Tsuru, T. G. 2008, PASJ, 60, 201

Koyama, K., Takikawa, Y., Hyodo, Y., et al. 2009, PASJ, 61, 255

Leccardi, A., & Molendi, S. 2008, A&A, 486, 359

Morrison, R., & McCammon, D. 1983, ApJ, 270, 119

Muno, M. P., Pfahl, E., Baganoff, F. K., et al. 2005, ApJ, 622, L113

Muno, M. P., Baganoff, F. K., Brandt, W. N., Morris, M. R., & Starck, J. 2008, ApJ, 673, 251

Muno, M. P., Baganoff, F. K., Brandt, W. N., Park, S., & Morris, M. R. 2007, ApJ, 656, L69

Murakami, H., Koyama, K., Sakano, M., Tsujimoto, M., & Maeda, Y. 2000, ApJ, 534, 283

Murakami, H., Koyama, K., & Maeda, Y. 2001, ApJ, 558, 687

Nakajima, H., Tsuru, T. G., Nobukawa, M., et al. 2009, PASJ, 61, 233

Nobukawa, M., Koyama, K., Tsuru, T. G., Ryu, S. G., & Tatischeff, V. 2010, PASJ, 62, 423

Nobukawa, M., Ryu, S. G., Tsuru, T. G., & Koyama, K. 2011, ApJ, 739, L52

Oka, T., Hasegawa, T., Sato, F., Tsuboi, M., & Miyazaki, A. 1998, ApJS, 118, 455

Oka, T., Tanaka, K., Matsumura, S., et al. 2010, ArXiv e-prints

Ponti, G., Terrier, R., Goldwurm, A., Belanger, G., & Trap, G. 2010, ApJ, 714, 732

Porquet, D., Predehl, P., Aschenbach, B., et al. 2003, A&A, 407, L17

Porquet, D., Grosso, N., Burwitz, V., et al. 2005, A&A, 430, L9

Predehl, P., Costantini, E., Hasinger, G., & Tanaka, Y. 2003, Astron. Nachr., 324, 73

Revnivtsev, M. G., Churazov, E. M., Sazonov, S. Y., et al. 2004, A&A, 425, L49

Schödel, R., Ott, T., Genzel, R., et al. 2002, Nature, 419, 694

Smith, R. K., Brickhouse, N. S., Liedahl, D. A., & Raymond, J. C. 2001, ApJ, 556, L91

Snowden, S. L., Collier, M. R., & Kuntz, K. D. 2004, ApJ, 610, 1182

Strüder, L., Briel, U., Dennerl, K., et al. 2001, A&A, 365, L18

Sunyaev, R., & Churazov, E. 1998, MNRAS, 297, 1279

Sunyaev, R. A., Markevitch, M., & Pavlinsky, M. 1993, ApJ, 407, 606

Terrier, R., Ponti, G., Bélanger, G., et al. 2010, ApJ, 719, 143

Tsuboi, M., Handa, T., & Ukita, N. 1999, ApJS, 120, 1

Tsuboi, M., Ukita, N., & Handa, T. 1997, ApJ, 481, 263

Turner, M. J. L., Abbey, A., Arnaud, M., et al. 2001, A&A, 365, L27

Valinia, A., Tatischeff, V., Arnaud, K., Ebisawa, K., & Ramaty, R. 2000, ApJ, 543, 733

Wang, Q. D., Dong, H., & Lang, C. 2006, MNRAS, 371, 38

Yusef-Zadeh, F., Purcell, W., & Gotthelf, E. 1997, in American Institute of Physics Conference Series, Vol. 410, Proceedings of the Fourth Compton Symposium, eds. C. D. Dermer, M. S. Strickman, & J. D. Kurfess, 1027

Yusef-Zadeh, F., Law, C., & Wardle, M. 2002, ApJ, 568, L121

Yusef-Zadeh, F., Muno, M., Wardle, M., & Lis, D. C. 2007a, ApJ, 656, 847

Yusef-Zadeh, F., Wardle, M., & Roy, S. 2007b, ApJ, 665, L123